University of BRISTOL

School of Chemistry

Fabrication and Evaluation of Beta Enhanced Diamond Thermionic Energy Converters

Ela Figanmese

This thesis is submitted in partial fulfilment of the requirements for the Honours Degree of BSc at the University of Bristol

Submitted April 2026

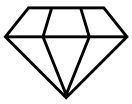

Supervisor: Professor Neil Fox

2nd Assessor: Professor Paul May

3rd Assessor: Professor Neil Allan

Statement of Factors Which Limited Project Progress

Due to some technical difficulties in the Bristol Diamond Lab, the amount of time left to complete all the intended experiments for this project was limited. Therefore, some experiments could not be conducted.

In October and November, access to equipment was limited due to maintenance in the air-conditioning system of the lab. Furthermore, due to an issue regarding gas storage all of the CVD reactors were shut down in January until this was resolved, which lasted for approximately three weeks. Shortly after that, there was a problem with the cooling system of the non-boron containing reactor which took an additional week to fix.

Due to these issues, the production of the first sample ready for analysis was completed in early February, two weeks before the lab-work deadline. Even with the additional lab time provided by Professor Neil Fox, there was only enough time left to use the NanoESCA once and conduct beta enhancement experiments only on hydrogen terminated diamond. This project originally intended on conducting beta enhancement experiments on metal oxide terminations as well, which would require more time in the NanoESCA. Instead of producing multiple samples to compare, only two identical samples Sample 1 and 2 were produced. Furthermore, due to limited time, they were used for different experiments: Sample 1 was used for thermionic emission tests and Sample 2 was used for characterisation in the NanoESCA. These samples were assumed to be identical but with more time it would have been more accurate to see if that is really the case by comparing them, which would involve characterising Sample 1 as well.

Abstract

Besides being a precious gem, diamond is also an invaluable material that can produce sustainable electricity. Thermionic Energy Converters (TECs) that use diamond emitters have the potential to convert heat from solar or nuclear sources into electricity. Diamond is a desirable emitter material because its electronic properties can be tuned to emit high volumes of electrons to the collector in a TEC configuration. This can be achieved by producing n-type diamond to lower the work function emission barrier and create a shallow donor level to fill the conduction band (CB) with additional electrons, allowing for more electrons to be emitted. Moreover, inducing a negative electron affinity (NEA) on n-type diamond, can eliminate the emission barrier between the CB and vacuum.

To create a n-type diamond with a NEA, two identical emitter samples (Sample 1 and Sample 2) were produced. On a polycrystalline diamond wafer, successive boron (B) and nitrogen (N) doped diamond layers were grown in a microwave plasma assisted chemical vapour deposition (MWCVD) reactor. The thickness of the B doped layer was 23 μm and the N doped layer on top of that was 1 μm thick. This method of co-doping was preformed to produce clusters such as BN_2 and BN_3 between the doped layers because it was previously predicted that these clusters create shallow donor levels. The effects dopants had on the quality of the diamond, was monitored by Laser Raman Spectroscopy after growing each layer on Sample 1. Both samples were hydrogen (H) terminated to create a NEA. The work function and NEA of Sample 2 were measured using Ultraviolet Photoelectron Spectroscopy (UPS). However, Sample 2 was charging so, the values of the UPS spectrum were offset by an unknown amount. Despite that, the high secondary electron peak at high binding energies qualitatively confirmed the existence of a NEA.

To promote even more electrons from the emitter to the collector, a Ni-63 collector was used because it is a beta particle source. Previous work has demonstrated that using Ni-63 collectors increased the maximum emission current density (MECD) produced, which was termed beta enhancement. In this study, the effects of beta enhancement were researched by using Sample 1 as the emitter with Ni-63 and non-radioactive Ni-59 collectors in a TEC configuration. During each TEC test, ten heating cycles from 300°C to 700°C were performed on Sample 1 to promote the release of electrons and to minimise H desorption. Nevertheless, in the Ni-59 control test H desorption caused the MECD to decrease overtime. Therefore, the highest MECD of 2.43 ± 0.07 μA cm^{-2} occurred in the first heating cycle at an emission threshold temperature of 563 ± 2°C. Conversely, in the Ni-63 tests beta enhancement caused the MECD to rise overtime, so the highest MECD of 1.75 ± 0.02 μA cm^{-2} was obtained in the last heating cycle with a threshold temperature below 300°C. A high enhancement factor of 6.27 was calculated for the MECD of the Ni-63 collector compared to the Ni-59 collector, during the final heating cycle. Beta enhancement could have occurred due to a combination of two effects. When the beta particles strike the emitter, electrons with higher kinetic energies can be released from the emitter preventing the formation of a space charge region in the interelectrode gap. Similarly, beta particles could impact the H atoms found in the emitter grain boundaries to re-terminate the surface after some of its original H-terminations desorbed. However, more experiments are needed to confirm the exact beta enhancement mechanism.

Acknowledgments

I would like to start off by thanking my supervisor Professor Neil Fox, who made this project possible in the first place. Exchanging ideas with him during our weekly group meetings and countless e-mails, guided me through this project. I am also very grateful for the extra lab time he provided, which allowed the results presented in this thesis to be complete. I would also like to thank Professor Paul May and Professor Neil Allan for providing me with further advice on how to construct this thesis.

I am grateful for Dr Ramiz Zulkharnay teaching me how to use the TECsim and CVD reactors. Beyond supervising me in the lab, I would like to thank him for his encouraging words that helped me navigate the challenging parts of this project.

I would also like to thank Mr Isaac Liu for his mentorship in the lab and for answering my endless questions. I am especially grateful for his help with designing the Ni collector holders and for mounting the beta radioactive Ni-63 collectors into the TECsim.

There were many unexpected technical difficulties in the Diamond Lab this year. Which is why I would like to thank Dr James Smith, who worked really hard on making sure that equipment was fixed as soon as possible.

I am also thankful for Dr Jude Laverock's help with carrying out measurements in the NanoESCA and subsequent guidance on data analysis.

The highlight of this project was sharing such a positive environment with everybody in the Diamond Lab office. Which is why I would like to thank Dr Liam Cullingford, Miss Catherine Monk, Miss Gulnur Zulpukarova, Miss Kisty Mao, Mr James Swarbrigg and all the project students. To my fellow BUDGies completing their final year projects, I am very grateful for all the lab chaos and laughter we shared this year. I wish you all the best after graduation.

Since this thesis was finalised towards the end of my degree, I would like to thank the people I had the pleasure of sharing these past three years with and who have been a constant motivation source while writing this thesis. Especially the University of Bristol A Cappella Society and my North Village friends.

Lastly, I would like to thank my parents for their endless support these past three years.

Table of Contents

1 Introduction

1.1 Thermionic Energy Converters (TECs)

Global annual electricity demand is projected to increase by approximately 3.6% per year until 2030. This growth in annual demand is on average 50% higher than the previous decade. These predictions have been strongly associated with the surge in air-conditioner usage due to rising global temperatures, transitioning to electric vehicles and constructing data centres to power artificial intelligence (AI).[1]

Therefore, providing reliable electricity to meet these growing demands while simultaneously reducing the usage of environmentally harmful fossil fuels, is a major challenge of the 21st century.[2] In pursuit of these goals, research has focused on developing sustainable electricity sources as well as improving the efficiency of existing energy conversion systems. Among these, Thermionic Energy Converters (TECs) have gained attention for their simple design and predicted high conversion efficiencies.[3]

A TEC is a vacuum diode device, as illustrated in Figure 1, and it consists of two electrodes separated by an interelectrode gap within a hermetic enclosure. The cathode is called the emitter because once it is heated, it releases hot electrons (also termed thermions) as part of a thermionic emission process.[3] These electrons pass the vacuum interelectrode gap before getting harvested by the colder collector, which is the anode. During operation, a potential difference between the two electrodes is formed because

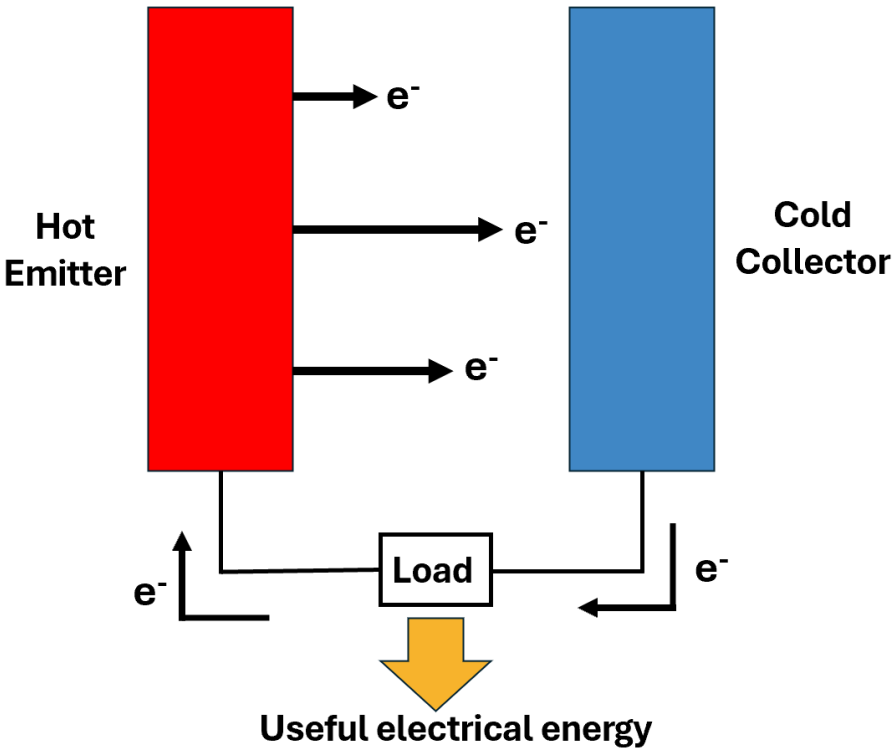

Figure 1 A schematic TEC set-up where the emitter and collector are separated by a vacuum interelectrode gap. An electrical wire connects these electrodes to drive a current through a load. This diagram was created with reference to Ref. 3.

the emitter releases electrons, whereas the collector accumulates them.[4] By connecting these electrodes, the circuit is completed and their potential difference can drive a current through a load which generates electricity.[5] Once these electrons flow back to the emitter, they can get re-emitted once more after gaining sufficient energy from the emitter that is continuously heated.[4]

From the operating principles of a TEC, it is evident that this static device can directly convert heat into electricity.[5] Therefore, it is a heat engine that uses electron gas as the working fluid.[6] The lack of mechanical components provides TECs with many advantages compared to conventional heat engines such as external combustion engines. For example, TECs eliminate irreversible friction losses, require little maintenance, have long operational lifetimes, tolerate high temperatures and operate in silence.[7]

1.1.1 Thermionic Emission

Thermionic emission, which is the fundamental operating principle of TECs, can be understood through band theory. Since the emitter and collector are made from solid materials, a large number of atoms interact in the lattice causing their distinct energy levels to become closely spaced such that they form continuous bands. In semiconductors, the valance band (VB) is usually partially or fully filled with electrons, whereas the conduction band (CB) is unfilled.[8] These two bands are separated by a band gap E_g, which is defined as the difference in energy between the valence band maximum (VBM) and the conduction band minimum (CBM).[9] Conversely, metals do not have a band gap and insulator materials have a band gap that is even wider than a semiconductor. The factors that determine this band structure are the chemical composition and crystal structure of the material.[8] The band diagram of a semiconductor material has been depicted in Figure 2.

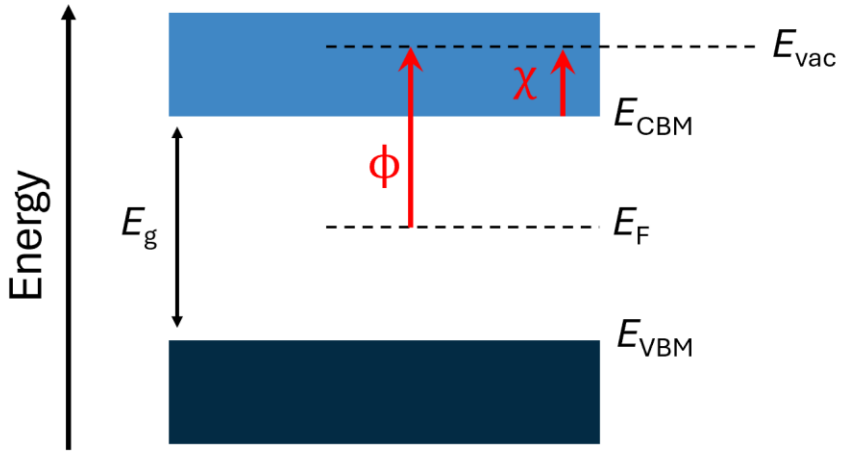

Figure 2 The band diagram of a semiconductor showing the work function denoted by ϕ and electron affinity denoted by χ. Since the vacuum level given by E_{vac} is above the energy of the CBM, E_{CBM}, this is an example of a semiconductor with a positive electron affinity. This band diagram was created with reference to Ref. 5.

Within the band gap resides the Fermi level E_F, which is defined as the electrochemical potential of electrons inside a solid. The E_F is a crucial electronic property because it affects the semiconductor work function, which is denoted by ϕ. The minimum energy required for an electron to get emitted from a surface, in other words the energy to overcome the potential barrier positioned at the surface-vacuum interface, is given by the work function. From Figure 2 it is apparent that ϕ is the difference between the energy of the vacuum level E_{vac} and E_F.[9]

In common electron emission processes electrons first need to be excited from the VB into the CB, by either thermal excitation or absorbing a photon with an energy equivalent to E_g.[10] For basic TECs, the latter occurs. However, as seen in Figure 2, the E_{vac} is commonly positioned above the CBM. This means that low energy electrons in the CB require additional energy to be emitted into vacuum. This energy barrier is given by χ in the band diagram which denotes the electron affinity, given by the difference between the energy of the CBM and $E_{vac.}$ In this case, the material exhibits a positive electron affinity (PEA).[9] The alternative and rarer negative electron affinity (NEA) pathway, which allows electrons in the CB to be emitted without an emission barrier, will be discussed in section 1.5.1.

In order to emit more electrons in a TEC, the emitter is heated to high temperatures. This can be understood from the Fermi-Dirac expression given in Equation 1, which calculates the probability of finding an electron *f(E)* at a certain energy *E*. Where k_B is Bolzman's constant and *T* is a certain temperature value.[11]

$$f(E) = \frac{1}{1 + e^{\frac{(E-E_F)}{k_B T}}} \tag{1}$$

By increasing the amount of heat applied into the system, the probability of electrons populating higher energy states will rise. As a result, it is more likely that electrons will have sufficient kinetic energies to overcome the work function barrier at the surface.[12]

Once the electron has been emitted from the material, the emission current density *J* can be calculated by the Richardson-Dushman equation. This is shown in Equation 2 where the temperature of the emitter is *T*, the work function of the emitting sample is ϕ and A_R is the Richardson constant.[13]

$$J = A_R T^2 e^{\left(-\frac{\phi}{k_B T}\right)} \tag{2}$$

From Equation 2 it should immediately become apparent that a high T and A_R, as well as a low ϕ, will contribute towards achieving higher emission current densities. The value of A_R is given by Equation 3 where Plank's constant is h, the charge and mass of an electron are given by e and m, respectively.[13]

$$A_R = \frac{4\pi m {k_B}^2 e}{h^3} = 120.2 \text{ A cm}^{-2} \text{ K}^{-2} \quad (3)$$

It should be noted that, Equation 3 was derived for metals with the assumption that the temperature and work function would be uniform across a surface. In reality, ϕ varies with temperature depending on a linear temperature co-efficient, given by α. So, to calculate a more accurate Richardson constant (A_R*) from A_R independent of temperature, Equation 4 can be used.[14]

$$A_R^* = A_R e^{-\frac{\phi\alpha}{k_B}} \quad (4)$$

1.1.2 Space Charge

Most electrons that have been released from the emitter do not have sufficient kinetic energy to reach the collector. Instead, they form an electron cloud in front of the emitter because they are attracted to the partial positive charge of the emitter, after it has ejected some of its electrons.[15] This decreases the emission current due to the space charge region imposing an additional energy barrier (E_{sc}) higher than the vacuum level onto electrons trying to escape the emitter as shown in Figure 3.[13] These detrimental effects become more apparent in high power applications intended for TECs, where lots of electrons are generated.[2]

To combat these issues, different methods to mitigate space charge effects have been researched. In the 1950s-1980s, due to the limited technology, wide interelectrode gaps of >100 μm were used, which are classified as macroscopic gaps.[16] To eliminate space-charge, the readily ionisable caesium (Cs) plasmas were used. These Cs^+ ions were able to mitigate space charge by neutralising the negative cloud of the space charge.[13] However, this required 50% of the output power to be lowered in order to maintain the Cs plasma.[17]

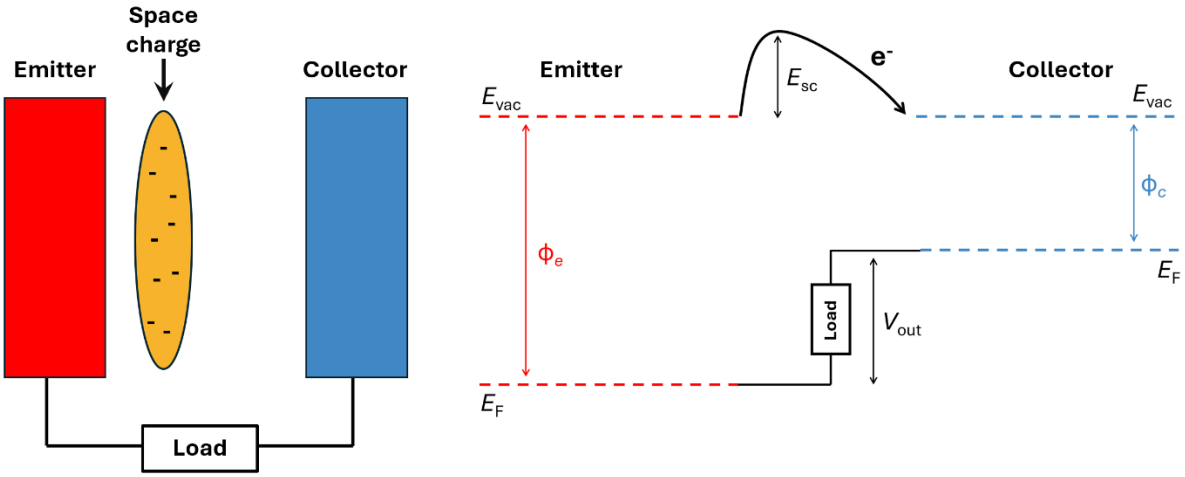

Figure 3 The space charge region that forms near the emitter in the interelectrode gap, created with reference to Ref. 3. Accompanied by an energy diagram of the electron emission process in the presence of an additional energy barrier imposed by the space charge, given by E_{sc}, adapted from Ref. 18.

Alternatively, the macroscopic gap can be made even smaller to assure that there will not be enough room for a significant amount of space charge to accumulate. It was found that interelectrode gaps in the micron region, at approximately <10 μm, are more efficient than Cs plasma TECs.[16] Therefore, careful considerations have been given to the development of gap engineering since placing the electrodes too close together may also result in reduced efficiency. For example, near-field radiative heat transfer starts to dominate when the interelectrode gap becomes smaller than the wavelength of thermal radiation. Consequently, parasitic heat loss increases and to compensate for that the emitter is further heated to maintain the power output.[16,19] This means that for a vacuum diode TEC configuration there is a trade-off between space-charge mitigation and minimizing parasitic heat loss. Therefore, the optimal gap for maximum efficiency should be determined by considering the balance between both factors.

1.1.3 Maximising Power Output

From Equation 2 it was clear that an emitter with a lower ϕ resulted in a higher emission current density. However, to maximise the output power generated by a TEC the emitter and collector work functions (given by ϕ_E and ϕ_C, respectively) need to have a potential difference. The output power density (P) of a TEC is given in Equation 5, where T is the temperature of the emitter.[14]

$$P = AT^2 e^{-\frac{\phi_E}{k_B T}}(\phi_E - \phi_C) \tag{5}$$

From Equation 5 it is evident that ϕ_E has to be low, but also not too low to be able to maintain a high work function difference between ϕ_C. For considerable output voltages to be achieved, the difference between ϕ_E and ϕ_C must be at least 1 eV.[4] To create a large potential difference, the ϕ_E needs to be raised with reference to ϕ_C, so that ϕ_C can have a relatively lower value and maximise output power.[14]

1.1.4 Carnot Efficiency

The maximum theoretical efficiency for all heat engines is given by the Carnot efficiency. The Kalvin-Plank statement of the Second Law of Thermodynamics reveals that it is impossible for a heat engine to achieve a conversion efficiency of 100%. This is because some heat must get rejected in order for a heat engine to do useful work.[20]

In the case of a TEC heat engine, electrons are the working fluid. The first step of the thermodynamic cycle involves the evaporation of electrons from a hot reservoir (the emitter) with a temperature of T_E. Some of the heat electrons gained from the emitter gets lost to the surroundings while the movement of electrons between electrodes does work. At the end of the cycle, electrons condense at the cold reservoir (the collector) at a temperature of T_C.[6] The Carnot efficiency (η) is given in Equation 5.[13]

$$\eta_{\text{Carnot}} = \frac{T_E}{T_E - T_C} \tag{6}$$

In order to obtain a high Carnot efficiency, the temperature difference between the emitter and collector has to be maintained to minimise the back emission of electrons from the collector to the emitter. This is difficult to achieve experimentally because as hot electrons contact the collector, they transfer their heat to it.[16] Furthermore, as the interelectrode gap shrinks near-field radiative heat transfer can also heat the collector.[19]

Despite these drawbacks, TECs have some advantages over other heat engines owing to their lack of moving parts. Conventional heat engines have temperature limits due to containing fuel combustion or mechanical stress as part of their energy conversion process. Thus, the emitters in TECs can be heated to elevated temperatures of 1600–1900 K, improving their efficiency. Furthermore, electron emission is a reversible process which raises the Carnot efficiency of TECs. This is to be contrasted with irreversible processes such as friction loss in other heat engines.[6] It has been predicted that TECs have a Carnot efficiency of 30% or higher.[21]

1.1.5 History of TECs

Thermionic emission was first discovered by T.A Edison in 1883, while he was researching incandescent lamps with carbon filaments. He observed that as carbon filaments were heated to produce light, the glass of the light bulbs would darken overtime. Edison theorised that negatively charged carbon particles were being "carried" from the hot filament, through the vacuum gap and depositing onto the glass. This was because he conducted experiments where he added a positively biased metal plate on top of the hot filament and measured a current flow, whereas there was no current flow with a negatively biased plate. This experimental set up has been shown in Figure 4a. Even though he was unable to fully understand why charge was carried across a vacuum, this phenomenon was historically termed the Edison Effect.[22,23]

The discovery of the electron by J.J Thomson in 1897 provided the missing puzzle piece to fully understand the Edison Effect. This inspired further research by O.W Richardson to investigate electron emission from hot surfaces. He provided a physical description for this phenomenon and formally termed it thermionic emission. Richardson's work on deriving the Richardson-Dushman equation, previously shown in Equation 2, earned him the Nobel prize in 1928.[24] Thermionic emission formed the heart of early electronics, since they were used in cathode ray tubes as well as vacuum tubes for radio and television transmission.[25] Schlichter recognised the importance of thermionic emission in heat to electricity conversion systems and filed the first patent for TECs in 1923.[12]

The mid-20th century marked an interest for the development of TECs in space applications due to their lightweight structure and ability to power long missions. The Soviet Union launched their nuclear space program through the development of TOPAZ I and TOPAZ II reactors. These reactors were named after the Russian acronym for

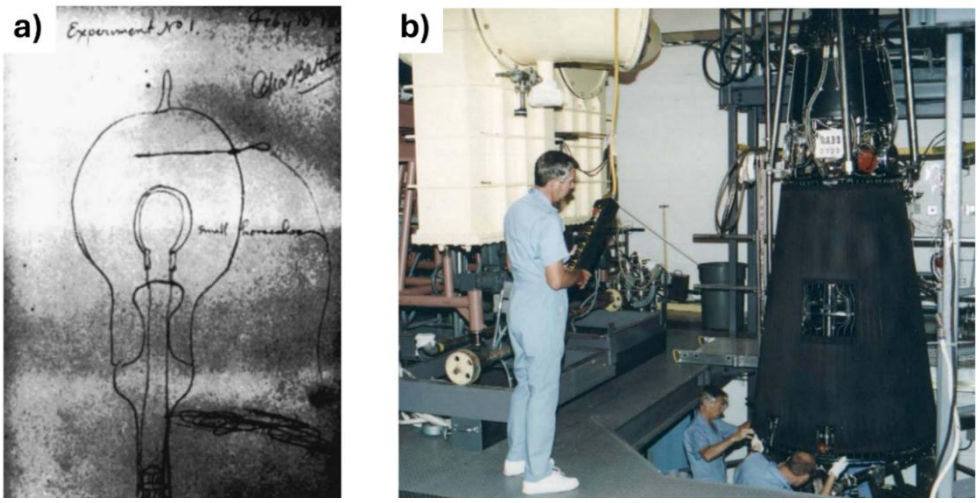

Figure 4 a) A page from Edison's notebook depicting the experimental set up he used to observe the negatively charged carbon getting "carried" across the vacuum. A biased metal plate was placed on top of the carbon filament to detect C particles. This image was taken from Ref. 22. b) Ground tests being conducted on the TOPAZ II reactor in the US as part of the TOPAZ-II International Program. This image was taken from taken from Ref. 26.

"Thermionic Experiment with Conversion in Active Zone."[3] The difference between these two reactors was that the TOPAZ I operated on a multi-cell thermionic fuel element (TFE), while the TOPAZ II had a single-cell TFE.[27] The first practical success of TECs occurred in 1987, when a TOPAZ I reactor with an electrical power of 6 kW was successfully launched to power a Soviet satellite for six months.[3,27] Following the Soviet's success, the U.S bought TOPAZ II reactors under the TOPAZ-II International Program (TIP). They aimed to use these reactors for a missile defence system called "Star Wars" and to potentially power lunar bases. Despite these plans the TOPAZ II reactor was never flight tested, but its ground tests, one of which is shown in Figure 4b, produced 4.5–5.5 kW of power which was considered a success.[27]

1.1.6 Modern applications of TECs

Since the 1980s, no practical success was reported for TECs due to significant efficiency challenges such as the formation of a space charge. In fact, the National Research Council amplified the scepticism towards the efficiency of TECs in a 2001 article titled "Thermionics Quo Vadis?"[3] Despite this negativity from the past, the advanced technology that exists today is capable of proposing novel devices that can provide sustainable electricity or power deep-space missions by harnessing the benefits of TECs.

1.1.7 Terrestrial Applications

The main advantage of TECs is their versatility, they can receive heat from a multitude of sources and convert it into electricity. These may be useful for terrestrial sustainable energy applications, since researchers have proposed to heat TECs by nuclear reactors.[7] TECs have also been considered in solar-cell applications. Significant research has been conducted in Stanford University to improve the electron emission process of basic TECs in a novel device called Photon Enhanced Thermionic Emission (PETE).[28]

Enhancement is achieved in PETE devices by combining the traditional approach of energising electrons into the CB through thermal energy, with the absorption of high energy photons as shown in Figure 5. Not only do PETEs enhance electron emission but also solve one of the main issues associated with photovoltaic (PV) cells: thermalisation losses. PV devices are made of semiconductors and when a photon with an energy higher than the band gap is absorbed, electrons are photoexcited into the CB. However,

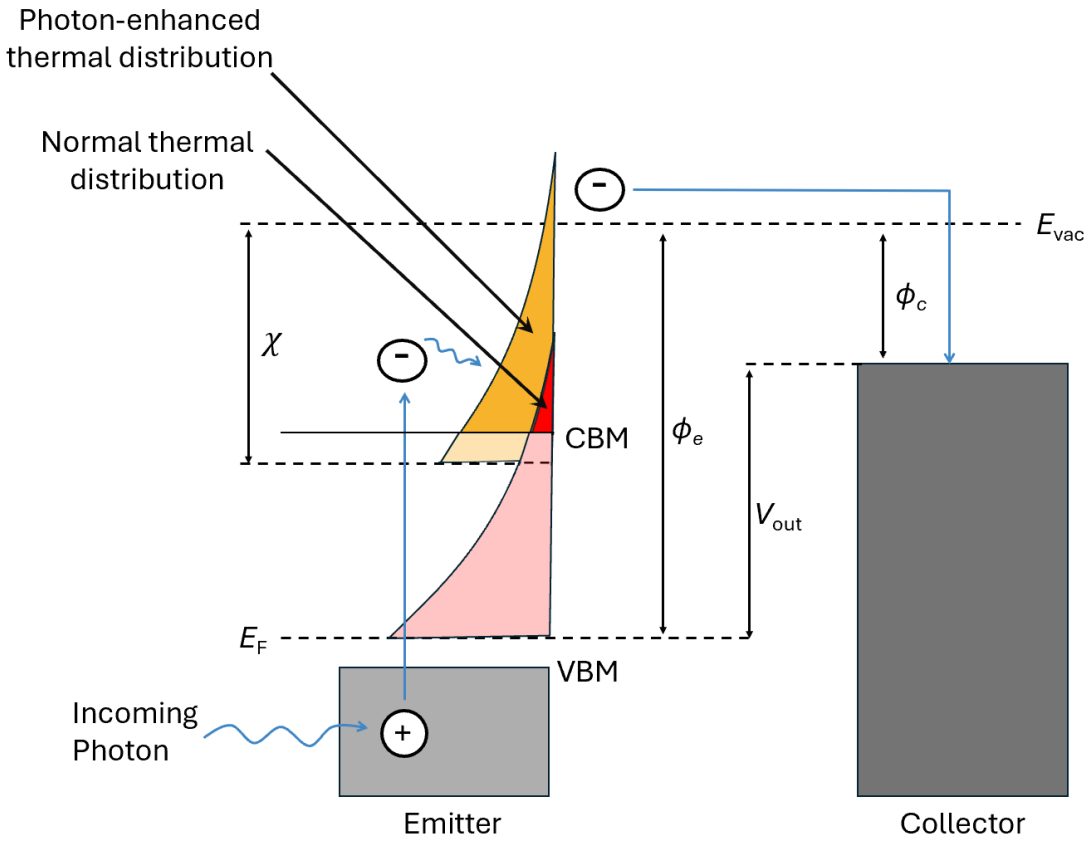

Figure 5 A schematic view of how a PETE operates. This image was adapted from Ref. 13.

electrons still have excess energy from the photon which is dissipated as heat by lattice scattering in a process known as thermalisation.[29]

In a PETE device, thermalisation becomes key in achieving higher efficiencies than PV devices. The CB gets filled by two processes that occur simultaneously: the photon-enhanced population and thermal population. The former occurs when the electrons in the emitter are photoexcited from the VB into the CB. The heat produced by thermalisation is used to excite electrons from the E_F into the CB to achieve the thermal population. At the CB, both population contributions combine and the electrons above the vacuum level are able to be ejected from the emitter.[28] With the help of PETEs, the 20% theoretical conversion efficiency of PV cells can be raised to 40% or even 50% when combined with a second thermal cycle.[29] To source photons, a solar tracking parabolic mirror can focus solar radiation onto the emitter of a PETE.[5]

Other terrestrial applications of TECs include enhancing the efficiency of existing power plants. The topping cycle of an external combustion engine involves burning fossil fuels which powers a generator to produce electricity. By adding TECs into the topping cycle, waste heat that is produced during combustion can also get converted into electricity. Thus, the Carnot efficiency of a combustion engine can be raised to 80% when used with a TEC.[6] Similarly, it has also been proposed to use the waste heat generated by

internal combustion engines in hybrid cars, to power the electric motor component using TECs.[30]

1.1.8 Space Applications

With space missions becoming increasingly longer in the pursuit of exploring deep-space, TECs are predicted to provide reliable long-term power in nuclear batteries for satellites.[27] Conventionally, nuclear batteries use a radioisotope thermoelectric generator (RTG) to convert the heat generated by radioactive decay into electricity.[31] However, the thermoelectric energy conversion process RTGs depend on are limited to a 10% practical conversion efficiency.[19] This value arises due to maximising thermoelectric conversion by generating a large Seebeck effect, which necessitates high electrical conductivity while maintaining low thermal conductivity.[32] TECs offer advantages over thermoelectric processes because the temperature difference between the emitter and collector is maintained by a vacuum gap, unlike the thermoelectric case where lattice thermal conductivity is an issue. Thus, TECs have higher predicted practical efficiencies because they can operate at higher temperatures.[19] Furthermore, switching from a thermoelectric process to a thermionic process shrinks the size of the device, which also provides a more lightweight alternative.[27]

Following the development of PETEs, they have been listed as potential candidates to power near sun space missions. In addition to the higher theoretical conversion efficiency of PETE devices compared to their PV counterparts, PETE devices can also tolerate higher temperatures of 673-1300 K.[33]

1.1.9 Materials for TEC Emitters

In order to turn the potential applications of TECs into a reality, research has focused on finding emitter materials that can produce high emission current densities. Therefore, materials with a high A_R and low ϕ are of particular interest. Table 1 summarises some previously researched materials for TEC applications.

Table 1 Work functions and Richardson constants of previously researched emitter materials for TEC applications

Emitter material	ϕ / eV	A_R / A cm^{-2} K^{-2}	Reference
W	4.54	55-104	34
Cs on W	1.36	3.2	34
BaO	1.5	0.1	34
Carbon nanotubes	2	110-120	34
Nanocrystalline diamond	1.29	0.84	34
Nitrogen doped diamond	1.99	70	34
Phosphorous doped diamond	0.67	2.3×10^{-7}	35

From Table 1 it is evident that the work functions of materials can be tuned. In the case of tungsten (W), depositing Cs on it reduces the work function significantly by 3.18 eV. Despite the low work function obtained by adding Cs on W, nanocrystalline diamond has an even lower work function. By adding phosphorous (P) impurities into the diamond lattice through doping, the work function of diamond can be further reduced to create an emitter with one of the lowest work functions reported in the literature. However, it also has an extremely low A_R.[35] In order to generate higher emission currents from diamond materials the nitrogen (N) doped diamond offers a good balance between low work function and high A_R.

Another advantage of diamond emitters compared to W emitters, is that they have a lower threshold temperature for electron emission. It has been reported that diamond emitters have a threshold temperature of approximately 900°C, whereas W emitters have threshold temperatures as high as 2000°C.[5] Due to these outstanding properties of diamond they have gained significant attention as potential emitters for TECs, which will be further explored in this thesis.

1.2 Diamond Materials

Carbon (C) has two naturally occurring allotropes, diamond and graphite, as illustrated in Figure 6. Diamond possesses some extraordinary material properties owing to the unique crystal lattice structure it is named after, diamond cubic. This structure consists of two close-packed interpenetrating face-centred cubic lattices, such that one lattice is shifted by ¼th of a cube along the cube diagonal. Thus, a 3D covalent network of sp^3 C is formed, which has the highest density among any solid with a value of 1.76×10^{23} cm^{-3}.[36] Diamond is also the hardest naturally occurring material with a mechanical hardness of approximately 90 GPa.[37]

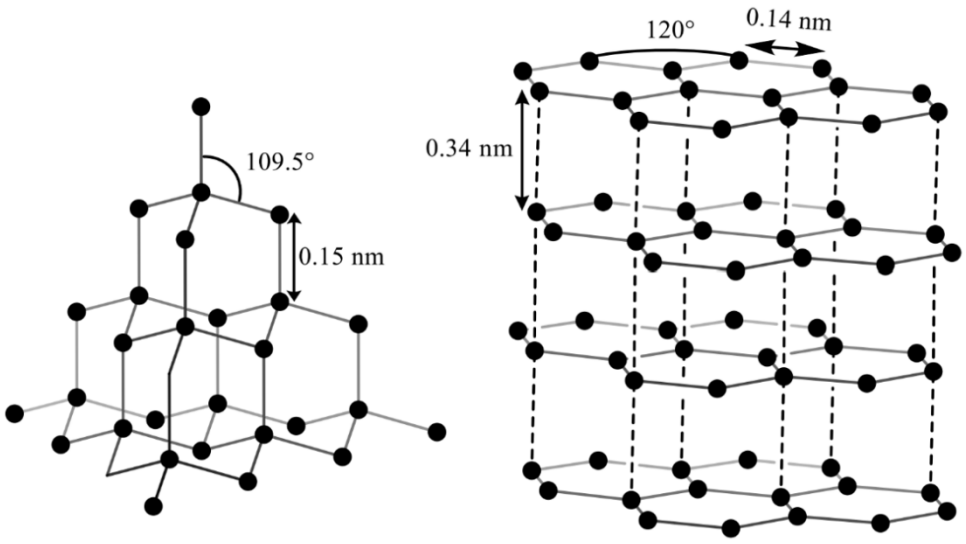

Figure 6 The natural allotropes of C where diamond is shown to the left and graphite is shown to the right. This image was taken from Ref. 38.

The C atoms in diamond are separated by short 0.154 nm single bonds that are held together strongly with a bond energy of 711 kJ mol^{-1}.[39] This rigid bond structure is significant because the vibration frequency of atoms in a lattice depend on their mass and the restoring force. The latter is related to the bond strength and is directly proportional to the vibration frequency, whereas the former is inversely proportional. Since diamond is made of relatively light C atoms that are strongly bonded, the atoms in the lattice vibrate at high frequencies. This is evident when comparing diamond to the heavier covalent network of silicon (Si), their maximum vibration frequencies are approximately 40×10^{12} Hz and 16×10^{12} Hz, respectively.[40] The high vibration frequency of diamond allows heat to be quickly dispersed along the lattice, resulting in high thermal conductivity.[39] The maximum thermal conductivity of diamond at room temperature is 2×10^3 W m^{-1} K^{-1}.[37] In fact, the thermal conductivity of diamond is such a unique property that thermal conductivity tests are commonly used by jewellers to assess the authenticity of diamond jewels.[41]

Furthermore, the chemical inertness and radiation resistance of diamond has allowed it to have applications under harsh conditions. For example, diamond sensors are under development for high intensity particle collider applications due to their resistance to radiation damage.[42]

1.2.1 Natural Diamond Growth

The natural formation of diamonds occurred more than three billion years ago, buried 140-240 km deep into the Earth's mantle. Reaching such depths causes the pressure and temperature to rise to 5.5–8.0 GPa and 1000–1400°C, respectively. Under these extreme conditions, the formation of diamond is favoured because it becomes the most stable C allotrope.[43] Once diamond is formed, it can be transported to the Earth's surface through volcanic erruptions.[44]

Instead of waiting for these slow natural processes to bring diamonds to the Earth's surface for mining, industry requires faster and larger-scale production of diamond. Moreover, natural diamond cannot be used in electrical applications because their material composition cannot be controlled.[45] This has given rise to producing lab-grown diamond, which is an ever-growing industry. In 2018 alone, China grew a total of 3600 tonnes (equivalent to 18 billion carats) of diamond which corresponded to 98% of the global diamond production.[46]

1.2.2 High-Pressure High-Temperature (HPHT)

The first successful attempt of producing lab-grown diamond was the high-pressure high-temperature (HPHT) technique developed by General Electric in 1955. This method uses graphite, which is the most stable allotrope of C under standard conditions (STP), as a C source to produce diamond under a pressure of 5–6 GPa and high temperatures of 1300–1600°C.[43] Since there is a high activation energy barrier between the conversion of graphite to diamond at STP, similar harsh conditions from the Earth's mantle had to be replicated in HPHT to favour diamond production as seen in Figure 7.[45] Once diamond has been produced, instead of converting to the stabler graphite phase, it will remain as diamond because it is meta-stable.[37]

Another key element of HPHT is the use of a catalyst to aid in diamond formation. Commonly, these consist of Fe, Ni, Co metal alloys. During growth, the graphite is placed in a cell containing a molten metal catalyst and a diamond seed. Once this cell is brought to growth conditions, the graphite diffuses through the molten metal and precipitates on the cooler diamond seed which grows the lattice further. However, due to their long

growth times and the presence of metal impurities in HPHT grown diamond, their use is limited to producing industrial cutting tools.[43]

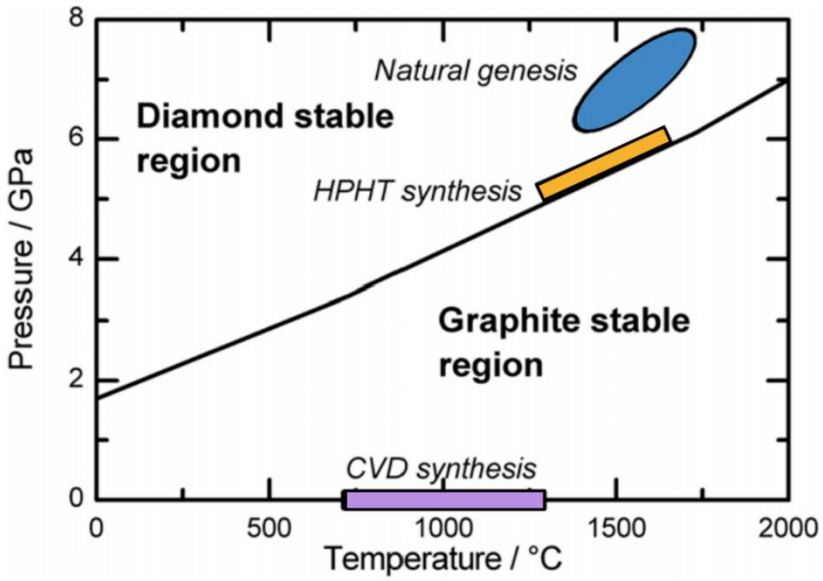

Figure 7 The phase diagram of C which shows the pressure and temperature conditions required for the natural, HPHT and Chemical Vapour Deposition (CVD) production of diamond. This graph was coloured from Ref. 45.

1.2.3 Chemical Vapour Deposition (CVD)

The harsh conditions used in HPHT were energy demanding, which drove the scientific community to research new energy-efficient diamond growth methods. Chemical Vapour Deposition (CVD) diamond growth emerged as a solution which grew diamond under a meta-stable regime, as shown in Figure 7, driven by kinetics rather than thermodynamics.[45] Due to this, the initial CVD method developed by Eversole and Deryagin had slow growth rates accompanied by low purities because graphite was getting co-deposited onto diamond. This issue was solved by Angus' group in the 1960s, where they used atomic hydrogen (H) during diamond growth to selectively etch graphite.[37] Thus, this group was able to grow diamond layers on natural diamond powder under milder conditions than HPHT, at a pressure as low as 0.3 torr and at a temperature of 1050°C.[36]

As the name suggests, CVD diamond growth consists of gas phase reactions that occur on top of an existing diamond surface in a stepwise manner.[37] To facilitate growth, a C containing gas like the commonly used methane (CH_4), or in some cases acetylene (C_2H_2), is mixed with excess hydrogen gas (H_2). This produces a feedstock for CVD growth containing ~1% CH_4.[47]

As this gas mixture in a CVD reaction chamber diffuses towards the substrate, they encounter an activation region. In order to initiate diamond growth, reactant gases need to fragment to from reactive ions, radicals and electrons. Activation can occur

thermally in Hot Filament CVD (HFCVD) or by an electric discharge in Microwave Plasma Assisted CVD (MWPCVD).[47] Even though these two techniques occur in different types of reactors, their gas content and reaction mechanisms are similar. Once these reactive fragments have formed, the ones that are adsorbed by a reactive site on the substrate surface can react in the mechanism illustrated in Figure 8.

The first step of the simplified diamond growth mechanism involves H abstraction from the diamond surface, using atomic H created during activation. This process produces H_2 gas and a reactive site with an incomplete valence called a "dangling bond." With the help of the excess H in the gas mixture, these can absorb and desorb from the dangling bond site to prevent the formation of graphite on the surface by hindering cross-linkage. This process continues until a (methyl) CH_3 radical binds to one of these reactive sites. Once the same reaction happens on a dangling bond next to the previously attached CH_3, an additional H abstraction on either of the bonded CH_3's can create a

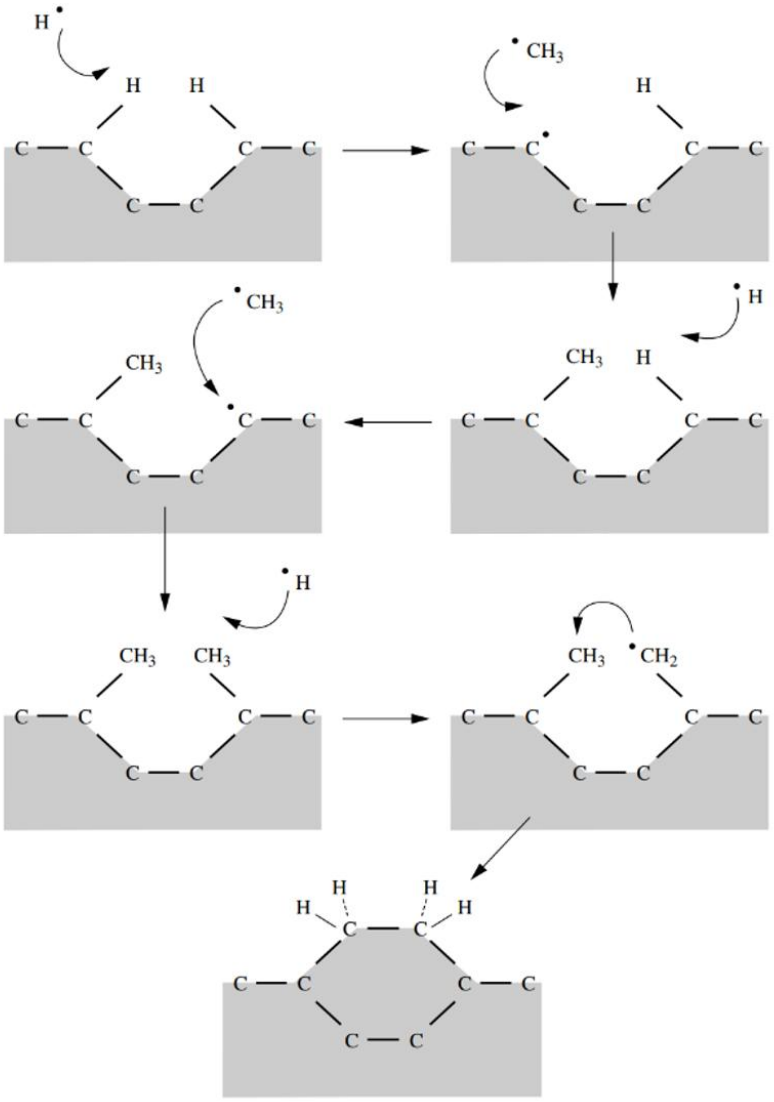

Figure 8 The simplified mechanism of CVD diamond growth which involves the stepwise addition of CH_3 onto surface diamond. This figure was taken from Ref. 37.

methylene (CH_2) radical. This newly formed radical can attack the adjacent CH_3 to form a ring which incorporates these two C atoms in the diamond lattice.[37]

CVD growth is a slow process because each step is reversible. Furthermore, any graphite that does end up depositing on the surface, H etches these preferentially compared to diamond. When long hydrocarbon chains are formed in the reaction chamber, while gases are mixing, H can also break these apart to prevent them from depositing onto the surface.[37]

1.2.4 Hot Filament CVD (HFCVD)

In HFCVD, electrically heated wires 5-10 mm above the substrate activate the gas mixture. These filaments are chosen to be materials with high melting points such as W, Ta or Mo.[47] Despite the filaments ability to reach temperatures as high as 2200°C, this maximum temperature is still limited by the melting point of the filament. Thus, the activated gas mixture reaches lower temperatures compared to its MWCVD counterpart and less reactive species are produced. This results in HFCVD having a lower growth rate than MWCVD.[40] Moreover, the grown diamond usually has some unavoidable ppm level metal contamination originating from the filament which prevents HFCVD films from being used in electronic applications.[37] Nevertheless, this is a low-cost technique and by increasing the number of filaments it can be scaled to produce diamonds with large surface areas.[47] A diagram of a HFCVD reactor is given in Figure 9a.

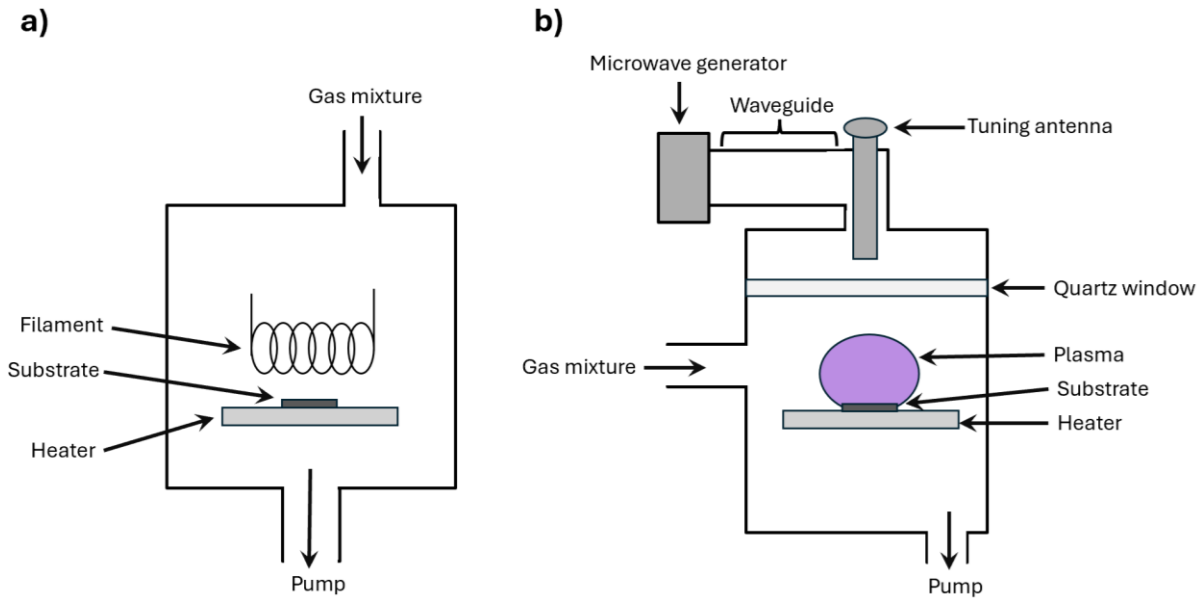

Figure 9 a) A diagram of the inside of a HFCVD reactor. b) A diagram of the components of a MWCVD reactor. Both diagrams were created with reference to Ref. 37.

1.2.5 Microwave Plasma Assisted CVD (MWCVD)

Plasma is the fourth state of matter, which consists of ionised gas, radical species and free electrons. Therefore, plasma species are encapsulated inside a highly energetic and reactive environment which can be controlled by the plasma pressure.[47] In high-pressure plasmas, electrons have a small mean free path which results in higher collisions with molecular species to form reactive H and CH_3. Even though the binding energy of H_2 is 4.5 eV, its dissociation peaks at higher electron kinetic energies of 25 eV. Due to this difference in the binding energy and electron kinetic energy, H atoms produced in MWCVD have significantly higher kinetic energies than HFCVD.[40]

MWPCVD stands out from other plasma-assisted growth methods owing to its ability to produce a higher plasma density which increases the quality of the diamond grown. For example, Radiofrequency CVD (RFCVD) is a lower frequency process because it discharges at 13.5 MHz, whereas microwaves discharge at 2.45 GHz in MWCVD. Thus, more atomic H and CH_3 radicals are formed in MWCVD.[40] Lastly, the absence of a filament above the substrate makes diamond grown by MWCVD pure and suitable for electronic applications.[37] Despite the high financial and energy costs of producing diamonds through MWCVD, once produced diamond TECs can last for a long time.

For a MWCVD reactor to work, microwaves must be introduced into the reaction chamber. The path microwaves follow has been illustrated in Figure 9b. From the microwave generator (or magnetron), microwaves follow a waveguide to the tuning antenna. These direct the microwaves towards a quartz plate, before introducing them into the reaction chamber for electric discharge. Gas flow is facilitated by gas inlets and exits through the exhaust lines.[48]

1.2.6 Diamond Orientations and Morphology

Lab-grown diamond can be produced in various forms such as single crystal diamond (SCD) or polycrystalline diamond (PCD). In SCD, a surface with uniform orientations is produced. These orientations are given by the Miller index which describes crystal planes through their interceptions with the x, y and z axes within a unit cell.[49] Especially the (100) and (111) orientations shown in Figure 10 are commonly used to grow

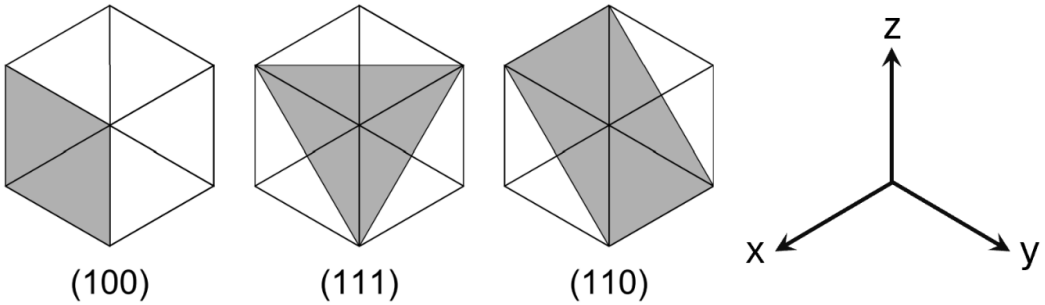

Figure 10 The (100), (111) and (110) orientations in a unit cell. A labelled axis was added next to the crystal planes taken from Ref. 51.

SCD in CVD diamond growth. Each crystal plane has different configurations of atoms at the surface, for example the (100) orientation has two unstable dangling bonds per surface atom. To lower the surface free energy, neighbouring atoms dimerise to form π bonds which corresponds to a (2 × 1) symmetry. This is to be contrasted with the (111) and (110) orientations that only have one dangling bond on each surface atom.[50] Therefore, the surface properties of diamond vary across different orientations.

On the other hand, PCD has no uniformity since it consists of randomly organised diamond grains with a specific orientation separated by grain boundaries. The grain size in PCD can be altered to form microcrystalline diamond (> 100 nm), nanocrystalline diamond (10-100 nm) and ultra nanocrystalline diamond (< 10 nm).[52] In high-quality electronic devices, SCD is preferred due to the absence of non-uniform current transportation present in their PCD counterparts. Research by Conte showed that the mechanism of current flow in PCD is non-uniform because it changes with temperature such that at lower temperatures, it is dominated by the grain boundaries and switches to the diamond lattice at higher temperatures.[53] Nevertheless, PCD is cheaper than SCD which has motivated researchers to maximise performance using PCD for electronic devices.[52]

1.2.7 Diamond as a Wide Bandgap Semiconductor

Despite diamond having a high thermal conductivity, it is also an electrical insulator. This is because diamond has a wide band gap of 5.47 eV, classifying it as a wide band gap (WBG) semiconductor.[54] In fact, diamond is often referred to as an “ultra” WBG material due to how significantly higher its band gap is compared to other WBG semiconductors such as 4H-SiC and GaN shown in Table 2. From Table 2 it is also evident that in terms of application benefits for devices, CVD diamonds show superior performance with the highest values for each property. Therefore, the development of diamond WBG materials is crucial since they have outstanding electronic properties which allows them to withstand harsh environments such as high temperatures, high power or high frequencies.[55] Diamond WBGs have potential applications in switches, power diodes, and unipolar field-effect transistors.[53]

Table 2 The properties of WBG semiconductors such as 4H-SiC, GaN and CVD diamond, compared to Si which is a conventional semiconductor. This table was adapted from Ref. 54.

Property	Si	4H-SiC	GaN	CVD Diamond	Device benefit
Bandgap / eV	1.1	3.2	3.44	5.47	High temperature
Thermal conductivity / W cm^{-1} K^{-1}	1.5	5	1.3	24	High power
Breakdown field / MV cm^{-1}	0.3	3	5	10	High voltage
Electron mobility / cm^2 V^{-1} s^{-1}	1450	900	440	4500	Performance speed
Hole mobility / cm^2 V^{-1} s^{-1}	480	120	200	3800	Performance speed

WBG materials such as diamond, AlN or cubic boron nitride have also been considered for next generation electron emitters due to exhibiting a NEA. Briefly, this property allows them to emit electrons into vacuum from the CB without experiencing a potential barrier. Therefore, the advantages of a NEA in WBG semiconductors overshadows the high energies required to excite electrons from the VB into the CB in the first place.[56] This is another reason why diamond is a suitable emitter for TEC applications. By tuning its material properties further, the ultimate potential of diamond as an electron emitter can be reached.

1.3 Constructing Diamond TECs

The already unique electrical properties of diamond can be altered to construct efficient TECs. This can primarily be achieved through two techniques: changing the bulk material properties by adding impurities through doping or by adding surface functionalisations on top of the diamond bulk.

1.4 Doped Diamond

Naturally occurring diamond is not made of purely C. During the formation of diamond, elements like N and boron (B) can also get incorporated into the lattice giving some natural diamonds their yellow or blue colours, respectively.[47] Beyond their beauty, the presence of B and N in the diamond lattice can also be useful in electronic applications by introducing charge carriers that increase the conductivity of diamond. B has one electron less than C, so it introduces positively charged holes through an acceptor level 0.38 eV above the VBM, creating a positively doped (p-type) material. Conversely, N has one additional electron compared to C which is why it donates electrons to the CB through a donor level 1.7 eV below the CBM producing a negatively doped (n-type) material.[57] The effects of B and N doping on the diamond band structure have been depicted in Figure 11.

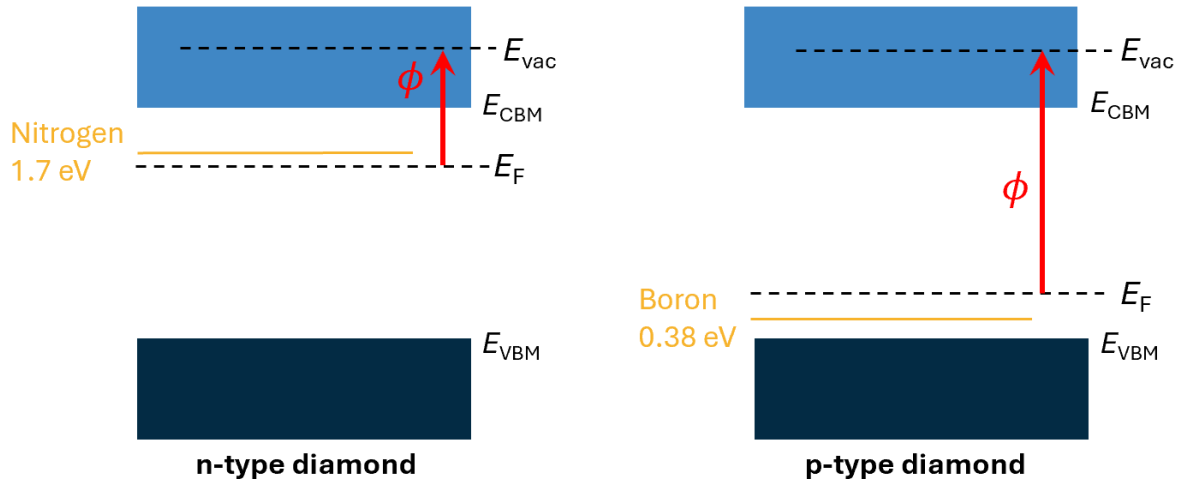

Figure 11 The band diagrams of diamond doped with N and B. The former is shown in the n-type diamond diagram to the right, and the latter is shown in the p-type diagram to the left. These diagrams were created with reference to Ref. 57.

These impurities found in natural diamond can also be incorporated into CVD diamond. In MWCVD, by introducing diborane (B_2H_6) and nitrogen gas (N_2) into the H_2/CH_4 gas mixture B and N doping can be achieved, respectively.[47] Substitutional dopants can be easily integrated into the diamond lattice if the atom has a similar atomic radius to C (0.77 Å) and has a high solubility which is controlled by the formation energy.[58,59] Due to the high density of the diamond lattice, this significantly limits the number of dopants that can be integrated into the diamond structure.[60] Therefore, N and B are of particular interest due to their similarity in size to C with atomic radii of 0.73 Å and 0.82 Å, respectively.[59] Thus, the lattice distortions imposed by B or N will have less internal strain compared to larger substitutional dopants, which allows them to have high formation energies.[59]

1.4.1 P-Type Diamond

The 0.38 eV acceptor level in B doped diamond (BDD) is considered shallow which means that a high volume of electrons in the VB can move into the acceptor level, generating holes in the VB.[61] This shallow acceptor state gives BDD its high hole mobility of 1840 $cm^2\ V^{-1}$ which explains why it can exhibit high electrical conductivity.[62] The conductivity of BDD can change from insulating to metallic by controlling the concentration of B.[63] BDD exhibits semiconductor-like conductivity at a concentration of 10^{19} cm^{-3}, when this is increased to 10^{20} cm^{-3} or higher it switches to metallic conductivity.[64] Despite the advantages of having a metal-like conductivity for BDD, heavy B doping damages the mechanical properties of diamond.[65]

1.4.2 N-Type Diamond

Compared to p-type doping, achieving conductivity in n-type diamond is a significant challenge.[66] This is attributed to two main factors: generating deep donor levels or the low solubility of atoms that could provide shallow donor levels. The former is the main issue observed with N doped diamond (NDD) because the 1.7 eV donor level is deep, which limits conductivity at room temperature requiring higher energies to promote electrons into the CB.[59] This is unfortunate because, as previously shown in Figure 11, n-type diamond has promising properties beyond enhanced conductivity as it can lower the work function by raising the E_F closer to the VBM.[56] A lower work function barrier is desirable for improving electron emission in TECs.

The advantages of n-type diamond in electron emission devices, has pushed research into finding alternatives for N to effectively create n-type diamond. Lithium (Li), was calculated to have an interstitial donor level 0.1 eV below the CBM.[59] Despite experimentally incorporating a high concentration, 1×10^{21} cm^{-3}, of Li into the diamond lattice, it was electrically inactive due to the mobility of Li.[67] Similar observations were made when doping diamond with sodium (Na), which had a predicted donor level 0.3 eV below the CBM. The reason behind the electrical inactivity of both atoms can be attributed to interacting with inactive aggregates or defects in the lattice as a consequence of their mobility.[59]

On the other hand, phosphorus doped diamond (PDD) displays relatively shallow donor levels at 0.57 eV below the CBM.[68] In fact, PDD is the most experimentally successful out of the n-type diamonds because, as previously shown in Table 1, Koeck and Nemanich were able to lower the diamond work function to 0.67 eV using PDD.[35] However, the larger size of P compared to C leads to more defects being formed in the crystal structure.[69] This explains why the A_R was low (2.3×10^{-7} A $cm^{-2}\ K^{-2}$) for the PDD reported in Koeck and Nemanich's work.[35] This is the unlucky fate shared with other heavy elements as well, for example arsenic (As) provides even shallower donor level at 0.4 eV

below CBM.[47,69] Thus, there is a trade-off between creating shallower donor states and reduced conductivity due to material defects.

1.4.3 Co-doped Diamond

Doped diamond is not limited to using one kind of dopant. Different kinds of small atoms can combine to form "clusters" within the diamond lattice, to alter its electronic properties. This technique is called co-doping and it is an active area of research because it may provide a pathway to finally producing a shallow n-type donor level.[69] This search is especially important for TEC applications to reduce the work function or to create diamond devices with p-n junctions.[56,70] However, experimentally co-doping is very difficult to achieve because multiple dopants need to be positioned next to each other to form clusters.[69]

For example, Moussa's computational studies on LiN_4 clusters (where Li was in the substitutional position tetrahedrally bonded to adjacent N atoms) showed that it was a potential candidate for n-type diamond because it produced shallow donor levels at 0.27 ± 0.06 eV.[66] Furthermore, tetrahedrally bonding the Li onto N was thought of as a possible way to reduce the mobility issue of the Li and improve results compared to the Li doped diamond experiment. However, Othman's study on co-doping Li and N in high concentrations reported low electrical conductivity. This could be due to either both dopants getting trapped in the grain boundaries or not achieving the computationally predicted doping ratio. In the case of the latter, further research is needed to achieve the theoretically calculated donor level.[67]

Alternatively, B and N which are commonly used dopant species in diamond can also produce clusters through co-doping. These atoms already unintentionally co-dope, due to the permanent contamination caused by using B_2H_6 in CVD reactors.[48] Computational experiments by Zhou have found that BN_2, BN_3, BN_4 clusters with B as the central atom, are potential candidates for n-type diamond. This research group predicted that among these clusters shown in Figure 12, BN_3 produced the cluster that had the highest solubility and shallowest n-type donor level of 0.23 eV.[59] This value is very low compared to position of the BN_2 donor level calculated by Moussa to be 1.19 eV below the CBM.[66] The predicted donor level for the BN_2 cluster is still shallower than N, but not as low as P. Therefore, Croot suggests that even though BN_2 and BN_3 are promising, they do not outweigh the properties of the experimentally successful P dopant.[69]

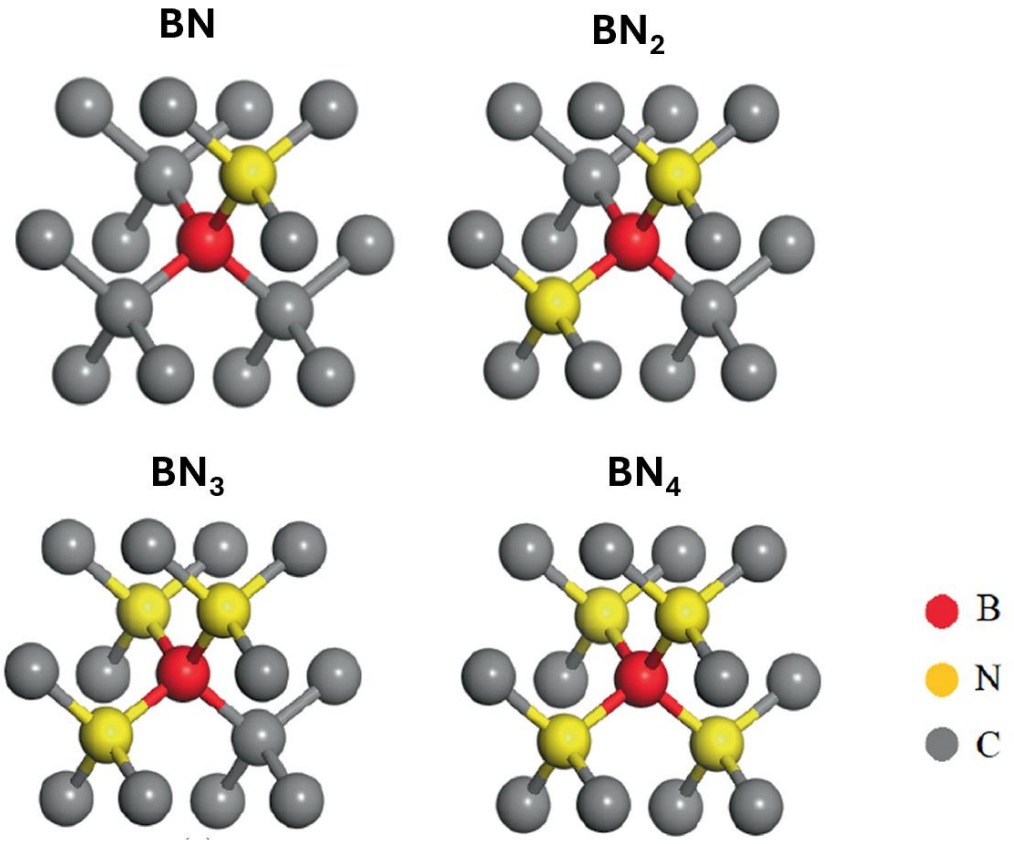

Figure 12 The configuration of the BN, BN_2, BN_3 and BN_4 clusters. This image was taken from Ref. 59.

The Liu group brought these calculations to life by conducting an experiment on B and N co-doped diamond. CVD growth on (100) orientated SCD was facilitated by introducing dopant gases B_2H_6 and N_2 into the chamber simultaneously. The B_2H_6/CH_4 ratio in the gas mixture remained the same at 50 ppm across all samples, whereas the N_2/CH_4 ratio changed between 0%, 2.5%, 5%, 7.5%, and 10% for different samples. Among these samples, the ones with N_2/CH_4 ratios of 5%, 7.5%, and 10% were identified as n-type diamond and produced donor levels between 0.8 and 0.9 eV below the CBM.[71] This finding is significant because it is one of the first successful productions of n-type diamond in literature.

These results by Liu's group can be improved by growing the B and N doped components separately through layered doping, instead of co-introducing dopant gases into the reaction chamber. Adding trace amounts of N_2 into a CVD reactor increases the growth rate of diamond, in fact adding 200 ppm N_2 demonstrates a ten-fold increase in the growth rate compared to N_2-free conditions. However, this effect can be hindered by co-introducing ppm level B_2H_6 into the growth chamber. Approximately one gas-phase B atom per 1000 N atoms is enough to display these detrimental effects.[48] In order to prevent this from occurring, it is possible to grow the B and N doped layers sequentially in dedicated B and N containing reactors. This growth method would still produce co-

doped clusters such as BN_2 and BN_3, due to the intermixing of the N and B doped layers where they are in contact. Thus, providing enhanced growth rates for the n-doped layer.

1.5 Surface Functionalisation

A more practical way of altering the electronic properties of diamond without worrying about dopant solubility into the bulk, can be achieved through surface functionalisation. The (2 x 1) surface structure of (100)-orientated bare SCD explained in section 1.2.6, is thermodynamically unfavourable in the absence of adsorbate atoms. Due to the abundance of H inside a CVD chamber, these can react with the C atoms on diamond (C_d) to create a (2 x 1) surface re-construction which results in H-termination.[72]

1.5.1 Negative Electron Affinity in Hydrogen Terminated Diamond

The commonly occurring H-termination of diamond during CVD growth, gives rise to a NEA. Unlike the case for PEA, electrons in NEA materials experience no barrier for emission once they have been excited into the CB because the vacuum level lies below the entire CBM. This phenomenon is called "true NEA" and has been depicted in the band diagram shown in Figure 13.[13]

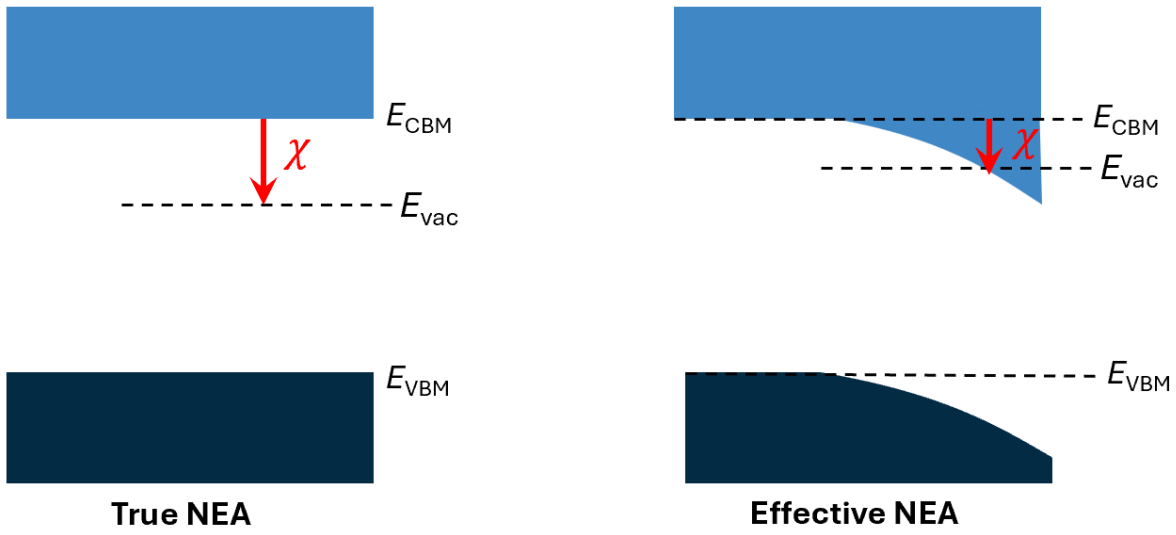

Figure 13 The band diagrams of true and effective NEAs created with reference to Ref.9.

The true NEA is to be contrasted with the "effective NEA" where band bending causes only part of the CBM to be above the vacuum level. When materials undergo surface reconstruction or termination, the E_F of the surface can differ from the bulk material. When a material has an electropositive surface termination with respect to the bulk, downward band bending occurs. This arises due to the CBM of the bulk being above the vacuum level and the CBM of the surface being below the vacuum level. Thus, surface

electrons experience an emission barrier due to the PEA and bulk electrons can reach the vacuum level owing to their NEA. This is also why a true NEA is desirable, since more electrons can get emitted.[9]

The electron affinity of materials can change when a surface dipole is formed. This is the case for H-terminated diamond which creates a NEA because of the surface dipole that is formed along the C_d-H bond, as a result of the electronegativity difference between C_d and H. Thus, a potential step where the vacuum level is pushed below the CBM takes place.[73] The electrons in the C_d-H bonds have a net movement towards the more electronegative C_d, where they are brought to the CB and emit spontaneously.[74] A NEA has been reported for H-terminated SCD with (100), (111) and (110) orientations at -1.3 eV, -1.07 eV and -1.0 eV, respectively.[75]

However, producing a NEA through H-termination has some drawbacks. For example, when it is exposed to ambient air the NEA will be lost due to partial oxidation whereby oxygen (O) or hydroxyl (OH) groups can replace the H.[76] Furthermore, H desorbs from the H-terminated diamond at temperatures above ~700 °C.[77] This is especially undesirable for diamond emitters in TECs that operate at elevated temperatures. Therefore, alternative NEA surface terminations that can provide air stability along with thermal stability at temperatures above 1000°C are under research.[10]

1.5.2 Metal and Metal Oxide Terminations

The Bristol Diamond Group has conducted significant research to find materials that are small and have a high electropositvity, as an alternative for H-termination. During this search, particular attention was given to Group I and II metals as well as first-row transition metals (TMs) that are less electronegative than C_d.[10] When metals are deposited directly onto diamond, it was found that carbide-forming metal adsorbates such as Ti, V and Al shorten the C_d-M bond. Thus, providing enhanced thermal stability as well as a NEA. However, this significantly limits the number of metals that can be studied for NEA research because most metals oxidise when exposed to air.[13]

To combat this issue, instead of a C_d-M bond, metals can be deposited on an already O-terminated diamond through thermal evaporation to form a C_d-O-M bond as shown in Figure 14.[77] This might appear paradoxical since O is more electronegative than C_d and induces a PEA. However, the metal is fully ionised when it is deposited on O, which means that the O-M creates a larger positive charge than the C_d-M bond at the surface. Thus, gives rise to a net NEA.[9]

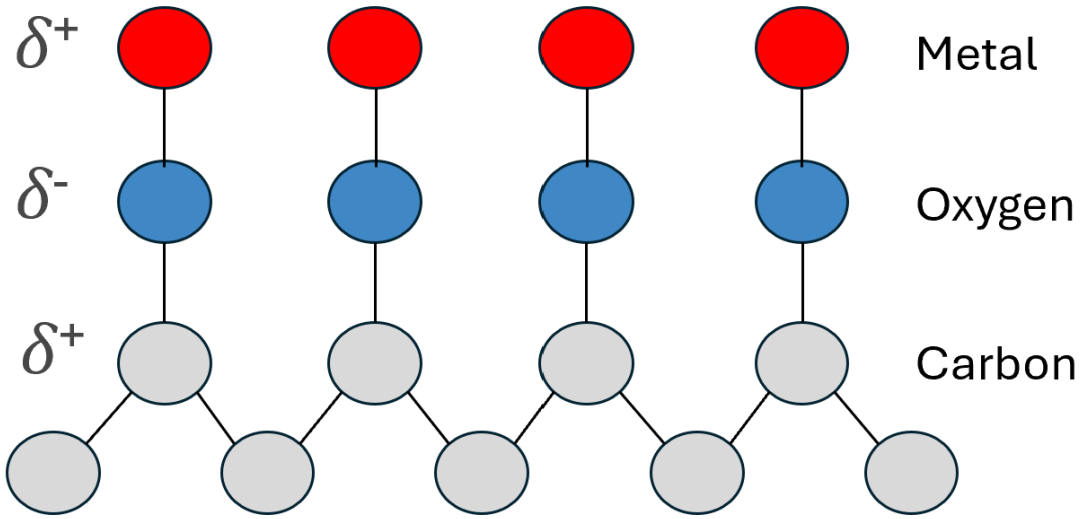

Figure 14 The surface arrangement of a C_d-O-M bond. Some examples of metals include Li or scandium (Sc). This image was created with reference to Ref. 78.

Air stability is achieved in C_d-O-M systems since the metal is partially oxidised which hinders further oxidation when it is exposed to ambient air.[10] Moreover, the O-M bond is ionic which has the ability to increase the surface dipoles even higher than H-termination.[77] Table 3 shows some experimental results from O-M terminations. [76]

Table 3 Different metal oxide terminations on (100)-oriented SCD with their experimentally obtained NEA and thermal stability values.

Metal oxide termination	Thermal stability / °C	NEA value /eV	Reference
LiO*	>925	-2.1	51
MgO	Unspecified	-2.01	79
ScO	Up to 700	-1.02	76
TiO	Unspecified	-0.9	10
AlO	Up to 800	Varies between 0 and -1	56

* = terminated on BDD.

Among the terminations in Table 3, LiO stands out as the best candidate to induce an NEA in TECs. This is because LiO has the lowest reported NEA as well as the highest

thermal stability. Thus, a diamond emitter that is LiO terminated should, in theory, produce a high emission current and operate at elevated temperatures. MgO has the second highest NEA, but more data is needed to confirm its thermal stability. O'Donnel has reported that no high-temperature annealing step was needed to activate the NEA of MgO, consequently as the sample was heated from 200°C to 700°C the NEA dropped to 0.9 eV.[79] This large drop in NEA does not make MgO suitable for TEC applications where a consistent NEA is required. Therefore, based off the other terminations in Table 3, ScO and AlO could be promising candidates for surface terminations in TEC applications owing to their moderately high NEA and thermal stability.

The emergence of O-M terminations highlights the need for uniform O-terminations with high surface coverages. This is because the electronic properties the O-M terminated surfaces depend on the O configurations such as ether (C-O-C), ketone (C=O), hydroxyl (C-OH).[80] Typically a mixture of all these O configurations are present in O-terminations. By altering the O-termination method certain configurations can get favoured. For example, ether bonds are favoured in both O_2-plasma (52.1%) and thermal crackling (71.5%) methods. Whereas acid-oxidation treatment produces hydroxyl (51.3%) and UV-ozone treatment favours ketone (47.9%) formation.[81] However, the percentages of these control methods still do not produce an O-terminated surfaces with a high surface coverage. Zulkharnay recently developed a new O-termination technique to solve this issue. This method is called "molecular oxygen" and produced an O-termination with a surface coverage of 90%. When a O-terminated (100)-orientated SCD was deposited with Li to form a LiO termination, the highest NEA achieved was -1.56 eV. Molecular oxygen has a higher NEA than obtained by UV-ozone, -1.31 eV, due to the low surface coverage associated with UV-ozone treatments.[77]

1.6 Beta Enhanced TECs

Recent studies by the Bristol Diamond Group have demonstrated an additional way of improving TECs, using beta radiation.[82] Beta radiation technologies have already gained significant attention due to their applications in beta-voltaic batteries that convert the kinetic energy of beta particles into electrical energy. In both TEC and beta-voltaic applications, by far the most preferred source is the Ni-63 radioisotope due to its long half-life of 100.1 years and emission of low energy beta particles, which are high energy electrons, with an average energy of 18 keV.[83] Thus, beta radiation powered systems have long operational lifetimes and produce beta particles in the decay reaction given by Equation 7.[84]

$$^{63}_{28}Ni \rightarrow {}^{63}_{29}Cu + e^{-} \qquad (7)$$

Ni-63 can be used as the collector in a TEC. Even though the exact behaviour of beta particles in a TEC is unknown, experimental results show higher emission from the emitter when it is exposed to beta radiation from the collector. In a 2017 study by Go *et al*, showed that the emission threshold temperature dropped by 58 ± 11°C in NDD emitter samples that were subject to beta radiation by using a Ni-63 collector, compared to samples that used a non-radioactive Ni-59 collector. Thus, beta-enhancement was observed. The ratio of the beta enhanced to non-beta enhanced emission current, provides an "enhancement factor" to show how much the emission current improved upon Ni-63 exposure. In Figure 15 the difference in emission currents between beta enhanced and non-beta enhanced cycles is visually apparent. The enhancement factor is also shown, which averaged at 2.7 between the 2nd and 20th cycle.[82]

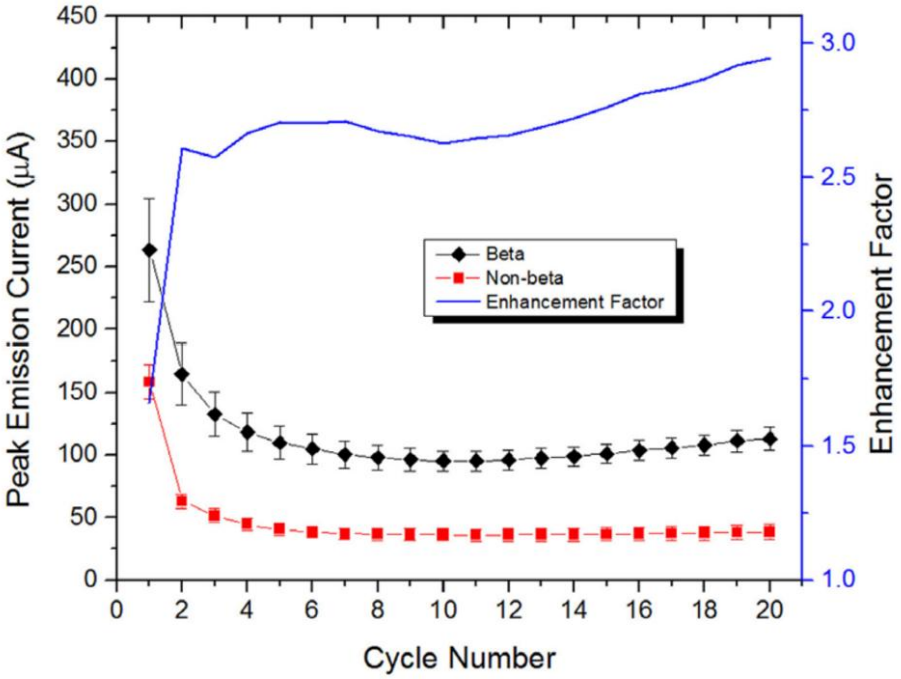

Figure 15 Comparison of beta enhanced and non-beta enhanced thermionic emission on Ni-63 and Ni-59 collectors, respectively. This graph was taken from Ref. 82.

Other research in the Bristol Diamond Group also observed similar results. For example, Bolton achieved 65% enhancement in emission current after using a Ni-63 collector with a NDD emitter.[84] Different explanations for beta enhancement have been proposed, but the listed ones were deemed unlikely to occur:

1) Collecting both thermionic electrons and beta particles at the collector.

Due to the positive bias applied on the collector during TEC tests, it was thought that the beta particles emitted by the collector were getting harvested alongside

thermionic electrons. However, both the beta enhanced and non-beta enhanced samples showed the same background current which disproved this.[82]

2) Secondary electron emission (SEE)

By transferring energy to surface electrons in the emitter upon beta particle impact, they can cause SEE. Thus, more electrons were thought to be collected. Even though SEE is very likely to occur, it would only provide a slight improvement to the emission current generated which is not enough to explain the high enhancement factors observed in experiments.[82]

3) Electron impact ionisation (EII) of H

The H-terminations were thought to enhance emission by desorbing and then getting ionised when colliding with beta particles to produce H^-, which would contribute to the current. Not only would the current decrease because H-terminations play a crucial role in forming the NEA, but also upon EII H atoms are more likely to become H^+ instead of H^-. In fact, the preferred production of H^+ would lower the current.[84]

On the other hand, the most likely explanation for beta enhancement relates to the Fermi-Dirac distribution. This equation was previously shown in section 1.1.2. When beta particles interact with electrons in the VB and CB of the emitter, through inelastic energy transfer they disrupt the pre-existing equilibrium of these electrons. As a result, these now non-equilibrium electrons will distort the Fermi-Dirac distribution and populate higher energy states to be emitted with higher kinetic energies, which enhances emission.[82]

1.7 Project Aims

This project aimed to produce an emitter for TEC applications, that is capable of releasing high volumes of electrons by producing n-type diamond with a NEA. Constructing successive B and N doped layers on diamond, attempted to produce BN_2 and BN_3 clusters between the doped layers to create n-type diamond. The NEA was produced by H-termination on the diamond surface. In order to further enhance electron emission, beta enhancement effects were studied on a beta radioactive Ni-63 collector and compared to a non-radioactive Ni-59 collector.

2 Methods

Two identical samples, Sample 1 and 2, that consisted of stepwise grown B and N doped layers (BNDL) on a PCD wafer, were studied. Both samples were H-terminated to induce a NEA. Due to time and equipment constraints, Sample 2 was used only for ultraviolet photoelectron spectroscopy (UPS), X-ray photoelectron spectroscopy (XPS) and energy filtered photoemission electron microscope (EF-PEEM) characterisation in the Bristol University NanoESCA Facility to determine the value of the work function and NEA as well as the surface composition. Whereas Sample 1 was used to compare beta enhanced (Ni-63 collector) and non-beta enhanced (Ni-59 and W collectors) TEC tests in the Thermionic Energy Converter simulator (TECsim) device. This experimental outline has been summarised in Figure 16.

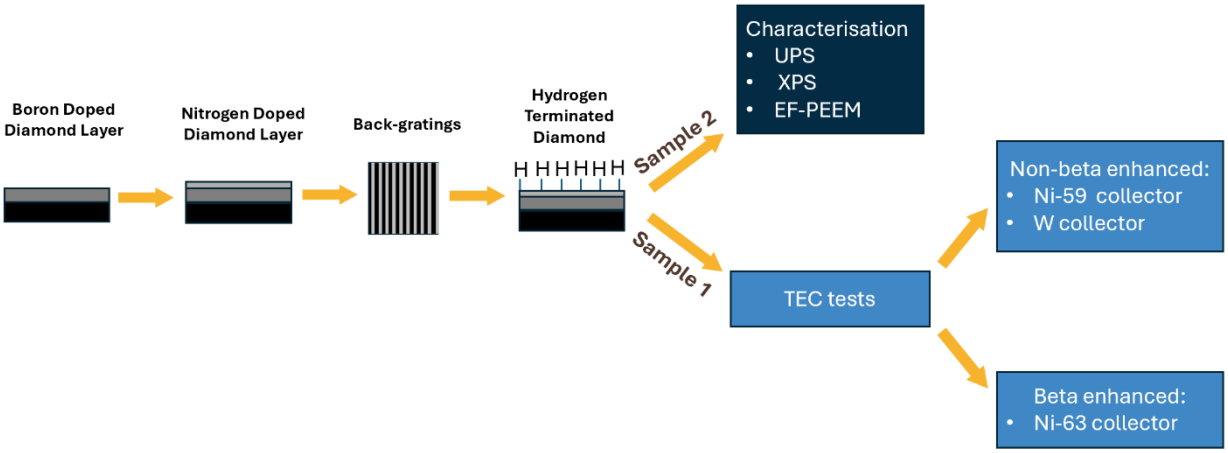

Figure 16 The experimental plan that produced two identical samples, Sample 1 and 2, which were used for TEC tests and characterisation, respectively.

The same diamond emitter, Sample 1, was used for all TEC tests despite studying different collector materials. Using the same emitter sample allowed for direct comparisons between beta and non-beta enhanced runs. Sample 1 was re-terminated every time a new experiment was conducted with a different collector in order to preserve the NEA. Furthermore, back-gratings were produced in order to maximise the laser absorption as the emitter was heated in the TECsim.

2.1 Sample Preparation

2.1.1 The Substrate

A 10×10 mm and 0.5 mm thick Element Six thermal grade TM100 PCD wafer (Product code: 145-500-0095) was used for growing doped layers. A diamond substrate was chosen instead of a non-diamond substrate, for a quicker growth process due to the omission of an initial seeding step. Some of the relevant properties of TM100 have been shown in Table 4.

Table 4 Properties of the TM100 wafer that were provided by the supplier, Element Six. This table was adapted from Ref.85.

Property at 300°C	Value in TM100
Thermal conductivity / W m^{-1} K^{-1}	>1000
Thermal expansion co-efficient / ppm K^{-1}	1.0 ± 0.1
Bulk resistivity / Ω cm	10^{12}
Surface resistivity / Ω cm	10^{10}

2.1.2 MWCVD

In order to minimise contamination caused by the B_2H_6 gas and thereby control the abundance of dopants between individual layers, both doped layers were grown in separate MWCVD reactors in the University of Bristol Diamond Lab. For the purpose of this thesis, to differentiate between the MWCVD reactors that preformed B and N doping, they will be called the "B reactor" and "non-B reactor", respectively.

Both reactors consisted of a home-built ASTeX-type MWCVD reactor that produced microwaves that had a frequency of 2.45 GHz, with the help of magnetron. The only difference between the non-B and B reactors was that they supplied 2kW and 3kW of power to the magnetron, respectively. To prevent damage to of reactor during growth at temperatures above 900°C, a water-cooling system ran through the reactor baseplate and walls.

2.1.3 Growing the Boron Doped Layer

Firstly, a B doped layer (BDL) was grown on the TM100 PCD wafer in the B reactor. At the centre of the reactor chamber baseplate, a 0.25 mm Mo separating wire was used to hold a Mo disk. The diamond wafer was placed on top of this disk. The chamber was isolated by closing the air inlet and put under a vacuum of 0.01 torr using an exhaust valve. The emissivity was adjusted to 0.15.

The inlet of gas and their concentrations were controlled by a LabView program. H_2 (300 sscm) was initially ejected into the chamber to produce a pressure of 15 torr. At this pressure, the power was brought to 0.65 kW allowing for the plasma to be struck

under these conditions. After the purple plasma was successfully produced, a ninety minute growth was facilitated according to the conditions outlined in Table 5.

Table 5 The BDL growth conditions used for Sample 1 and 2 in the B reactor. The temperature varied between each separate growth but was kept at approximately 1050 ºC degrees.

Parameters	Measured during growth
Temperature	~ 1050ºC
Power	1.10 kW
Pressure	110 torr
Emissivity	0.15
CH_4 flow rate	12.5 sscm
H_2 flow rate	300 sscm
B_2H_6 flow rate	0.3 sscm
Duration	90 min

The reflective power of the magnetron was conserved at approximately 0 kW by turning the tuning rods. A Raytek Thermalert SX optical pyrometer, allowed for temperature measurements during growth. In Figure 17, the B containing reactor and a top-down view of the diamond wafer engulfed in plasma has been shown.

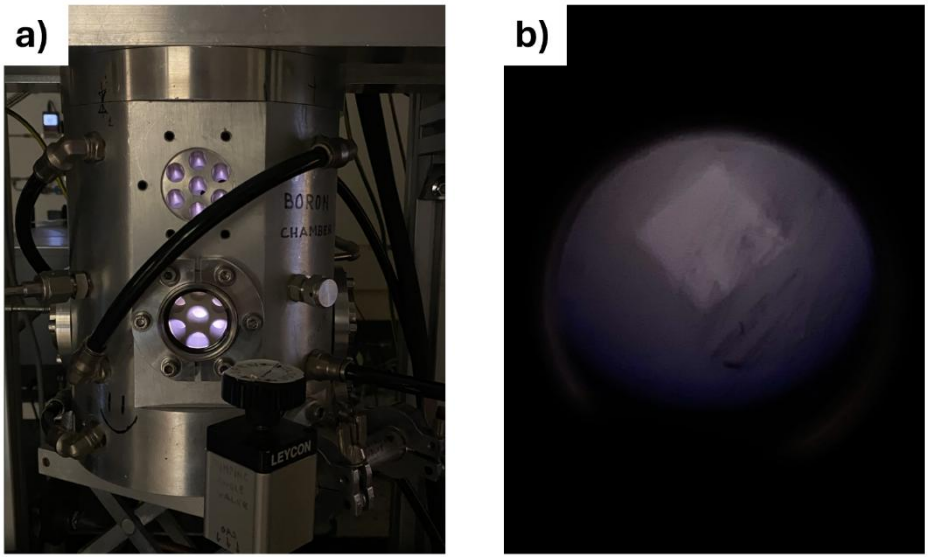

Figure 17 a) The Bristol Diamond Lab's B reactor during operation. b) The TM100 diamond wafer surrounded by plasma during BDL growth.

2.1.4 Growing the Nitrogen Doped Layer

Once the BDL was formed, the N doped layer (NDL) was grown on top of it in the non-B reactor, shown in Figure 18a. A Mo disk was placed on top of a 0.20 mm Mo separating wire for growth. Once the sample was loaded on top of the disk, the same steps used in the B reactor were followed except with different growth parameters as

given in Table 6. During growth, the $H_2/CH_4/N_2$ plasma showed a predominantly bright blue/green colour due to the introduction of N_2 as shown in Figure 18b.

Table 6 The NDL growth conditions used for Sample 1 and 2 in the non-B MWCVD reactor.

Parameters	Measured during growth
Temperature	~ 950°C
Power	1.30 kW
Pressure	130 torr
Emissivity	0.15
CH_4 flow rate	12.5 sscm
H_2 flow rate	300 sscm
N_2 flow rate	4 sscm
Duration	15 min

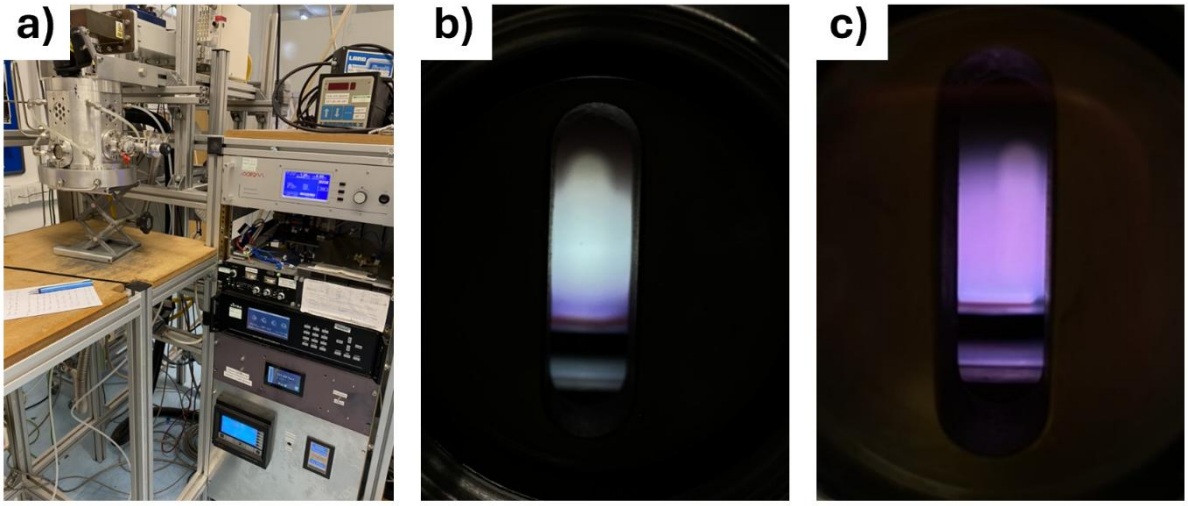

Figure 18 a) The Bristol Diamond Lab's non-B reactor where the manual gas flow, temperature and power controls can be seen. b) The blue/green coloured plasma observed while growing the NDL due to the presence of N_2. c) The purple colour of the H_2 plasma observed during H-termination.

2.1.5 Hydrogen Termination

The final BNDL diamond was H-terminated in the non-B reactor to produce a NEA on the surface. This procedure has been summarised in Table 7, consisting of a three-step process in which each step took two minutes: Surface cleaning, H-termination and cooling. In the first step, any non-H terminations to the diamond surface were removed by exposing it to a H_2 plasma under high pressure and power. This helped the next step, to make sure all sites could be terminated with H instead. The purple H_2 plasma was shown in Figure 18c. Lastly, in the cooling step, the newly formed H-bonds were allowed to stabilise under an H_2 environment in the absence of plasma.

Table 7 The conditions for H-termination that were used before each TEC test for Sample 1 and prior to the characterisation of Sample 2.

Step	Pressure / torr	Power / kW	Temperature / °C	Time / min
Surface Cleaning	130	1.3	~ 950	2
H-Termination	50	0.70	~ 550	2
Cooling	30	0	~ 20	2

2.2 Characterisation

2.2.1 Laser Raman Spectroscopy

Laser Raman Spectroscopy is a non-destructive technique used to assess the C phases formed during diamond growth because it is sensitive to both sp^3 and sp^2 C. It is a type of vibrational spectroscopy technique in which Raman active molecules polarise the electron cloud.[86]

Raman peaks are formed when monochromatic light excites electrons into virtual energy states, as shown in Figure 19. This can occur in two ways: Rayleigh scattering and Raman scattering. The former is elastic light scattering, whereby the excited electron falls back to the same energy level it started in. Thus, the monochromatic light and the scattered light produced by this excitation have the same wavelength.[86]

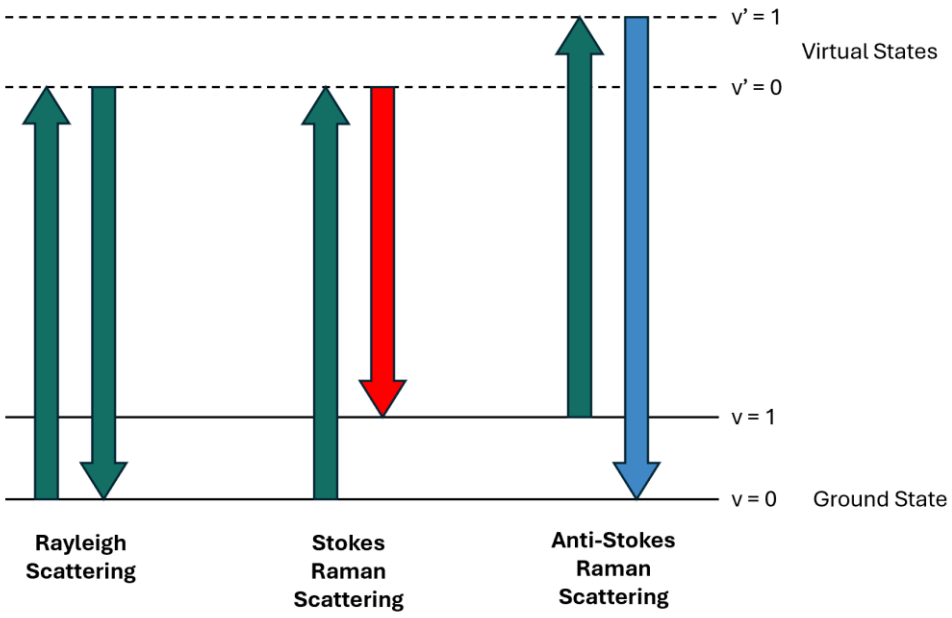

Figure 19 The energy diagrams depicting electron excitations for Rayleigh Scattering, Stokes Raman Scattering and Anti-Stokes Raman Scattering. Created with reference to Ref. 9.

Conversely, Raman scattering is an inelastic process. The excited electron may drop to either a higher or lower vibrational state than what it started with, which are termed Stokes Raman Scattering and Anti-Stokes Raman Scattering, respectively. Stokes Raman Scattering produces a photon with a longer wavelength than the monochromatic light, whereas the Anti-Stokes Raman Scattering produces a shorter one. The change in wavelength of the scattered photon is significant because it reveals information on the vibrational frequency of the atoms, allowing for the atomic composition to be determined. Since Stokes Raman Scattering has a higher intensity than Anti-Stokes Raman Scattering, Raman spectra are typically based off Stokes Raman Scattering.[9]

In a Raman spectrometer, first the sample was shined with monochromatic light, which produced either Raman or Rayeleigh scattering. This scattered light was carried to a filter through a beamsplitter where the Rayeleigh scattering was removed. The remaining Raman scattered light was then directed to a diffraction grating where its different wavelengths were separated. This allowed for the detector to identify atomic species and their intensities.[87] The laser pathway taken during measurements has been illustrated in Figure 20a.

The Renishaw 1000 Laser Raman Spectrometer used for data collection has been shown in Figure 20b. It was equipped with an Ar^+ laser that produced green monochromatic light with a wavelength of 514 nm. This laser wavelength was chosen because it is sensitive to both sp^3 and sp^2 C.[86] On the Windows-based Raman Environment (WIRE 2.0) software, the laser output was adjusted to 33% and the accumulation time was set to 10 seconds to optimise the signal-to-noise ratio during

data acquisition. The spectra were also centred at 1332 cm^{-1} to identify diamond. From this data, the baseline of the spectrum was removed and the full-width half-maximum (FWHM) of the diamond peak was calculated using a Lorentzian fit on OriginLab.

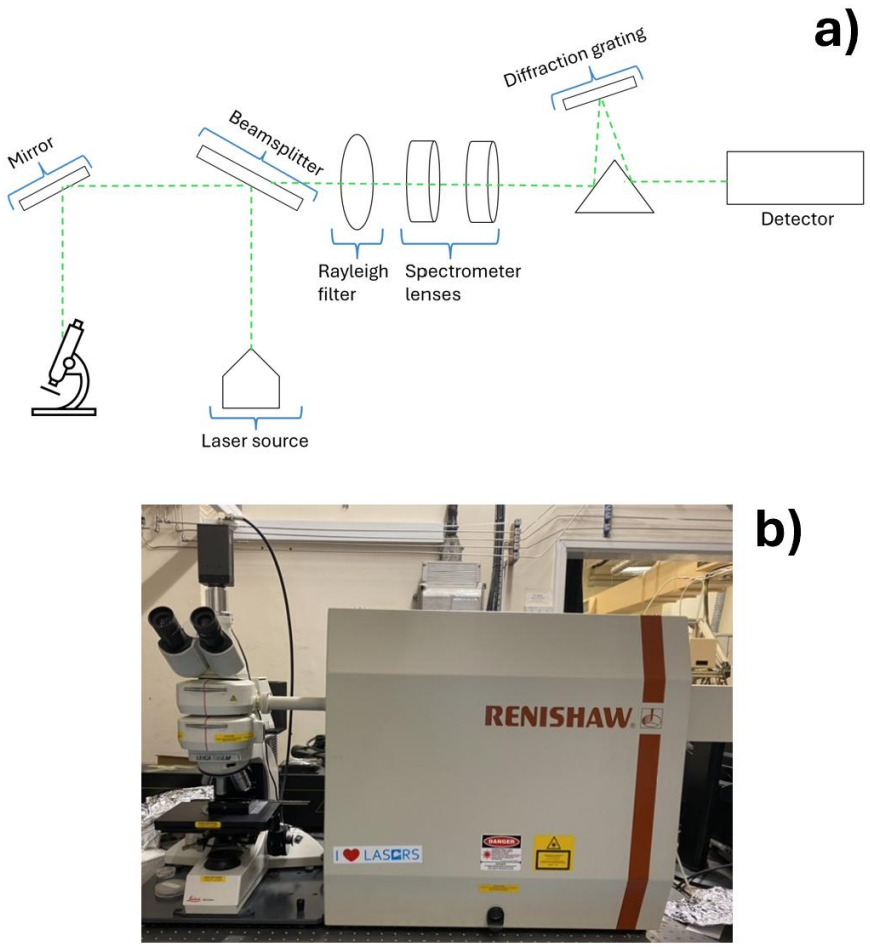

Figure 20 a) A diagram depicting the pathway of the laser and scattered light inside a Raman spectrometer. Created with reference to Ref. 87. b) The Renishaw 1000 Laser Raman Spectrometer in the Bristol Diamond Lab.

2.2.2 NanoESCA

In order to analyse Sample 2 by UPS, XPS and EF-PEEM the NanoESCA was used. There, the sample was kept under ultra-high vacuum (UHV) of approximately $1x10^{-8}$ Pa. It was transported between different analysis chambers for characterisation, as shown in Figure 21.

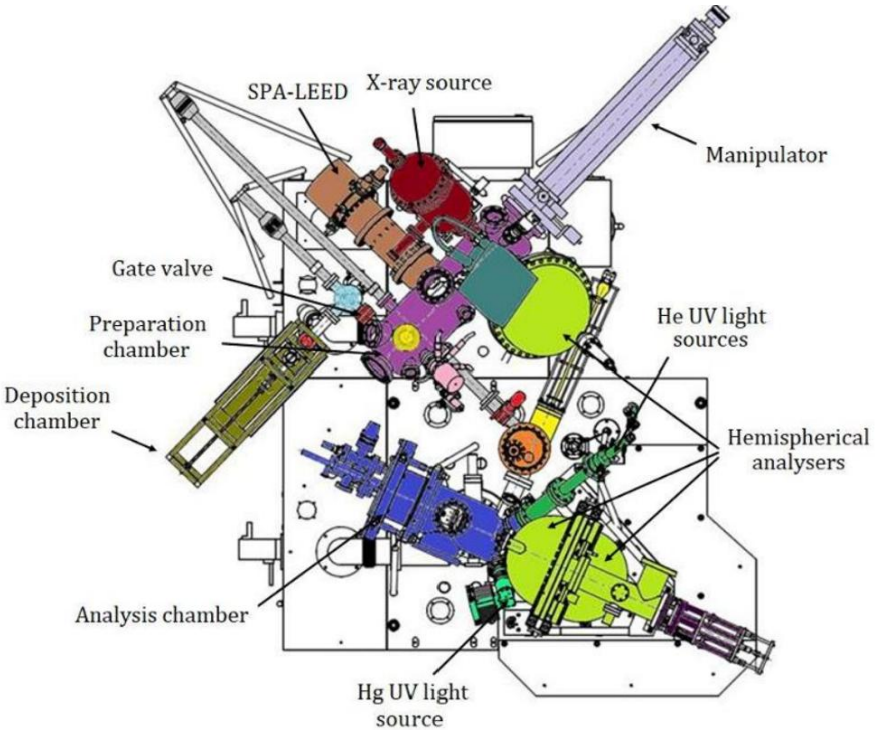

Figure 21 The different analysis chambers found in the Bristol NanoESCA facility. This image taken from Ref.72.

Prior to analysis, Sample 2 was first annealed in the preparation chamber for one hour at 300ºC, with a 2.26 A current passing through the sample. This process helped remove any surface adsorbates from the sample that may have caused contamination.

2.2.3 Photoelectron Measurements

The photoelectric effect is the main principle behind the operation of EF-PEEM, XPS and UPS measurements. This occurs when photons with energies that exceed an electron's binding energy and work function are absorbed, allowing the electron to use the remaining energy for emission into vacuum with some kinetic energy. This relationship has been depicted in Equation 8 where $h\nu$ is the energy of the photon, E_{BE} is the binding energy of the electron, ϕ_s is the work function of the sample and E_{KE} is the kinetic energy of the electron when it is released from the sample.[88]

$$hv = E_{KE} + E_{BE} + \phi_s \quad (8)$$

Both XPS and UPS techniques are surface sensitive which means that only the electrons near the surface can get analysed. Despite an incident photons' ability to penetrate a few microns deep, electrons lose their energies as they travel inside the material due to scattering.[89] This can occur in various mechanisms such as trapping, recapture or inelastic collisions.[86] Surface electrons are less likely to be subject to these mechanisms, therefore have sufficient energy to get emitted. Furthermore, the UHV chamber in the NanoESCA was used to prevent collisions between emitted electrons and gas molecules. Otherwise, these collisions would lower the energy of electrons resulting in no detector signal from the electrons.

2.2.4 X-ray Photoelectron Spectroscopy

XPS can analyse the bonding and chemical composition of near-surface atoms, except for H and helium (He). The high energy of X-ray photons, allow for core electrons to get emitted.[88] Since XPS is concerned with the bonding environment of atoms, the electrons that arrive at the detector with certain kinetic energies are converted to binding energies. Different binding energies are obtained due to different polarisations and chemical potentials induced by atoms. Thus, binding energy values correspond to unique chemical environments.[90] The binding energy can be calculated by the relationship shown in Equation 9, where ϕ_d is the detector work function. Since ϕ_d and hv are known, while the kinetic energy can get measured, this means that the binding energy of a sample can get calculated.[88]

$$E_{BE} = hv - E_{KE} - \phi_d \quad (9)$$

In the NanoESCA, fixed-energy X-rays were generated using a monochromatic Al Kα X-ray source with a photon energy of 1486.7 eV. The laser was shined directly above the sample. A wide-range survey scan with a pass energy of 50 eV, as well as individual scans centred on the C 1s, O 1s, N 1s and B 1s core levels with a pass energy of 20eV were analysed. This data was analysed in CasaXPS using a Shirley background.

The XPS in the NanoESCA and a schematic explanation of how it operates has been depicted in Figure 22. XPS used a hemispherical analyser to determine the kinetic energies of photoelectrons. By applying a voltage to the hemispherical analyser, only electrons with certain energies can travel through it. The outer and inner hemispheres were negatively and positively charged, respectively. This voltage can be altered to allow

for electrons with different energies to be analysed. Analysers with larger radius' have enhanced energy resolution which is important for obtaining accurate measurements.[88]

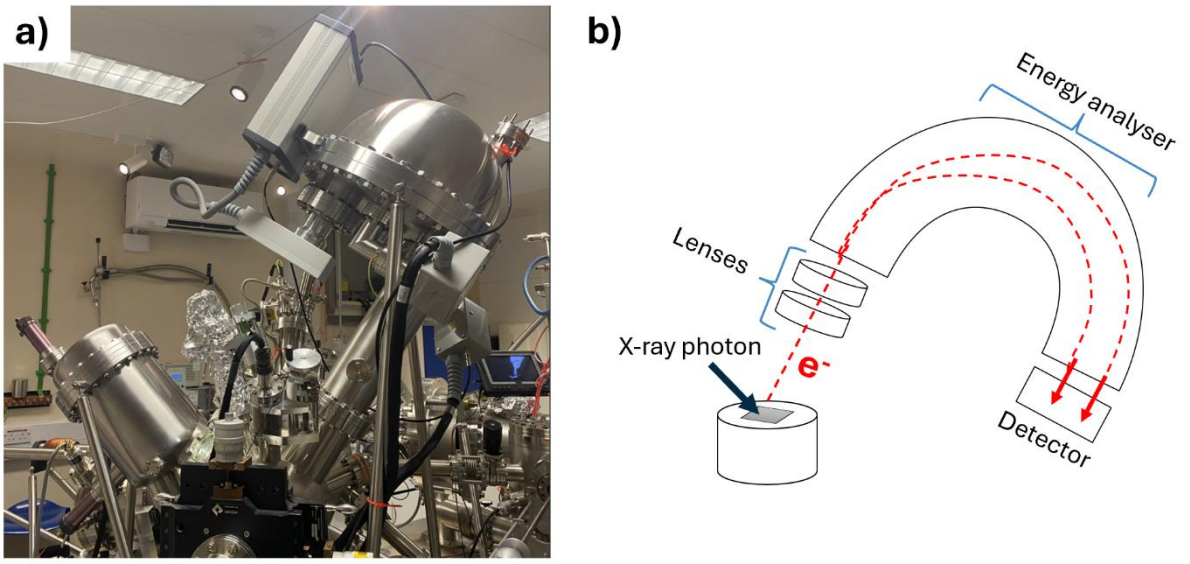

Figure 22 a) A picture of the XPS inside the NanoESCA. b) A diagram explaining the operation of an XPS, created with reference to Ref. 72.

2.2.5 Ultraviolet Photoelectron Spectroscopy

UV photons have less energy compared to X-ray photons, therefore they have sufficient energy to eject valence electrons into vacuum. Obtaining UPS measurements occurs in steps, as illustrated in Figure 23. Firstly, the electrons in the VB get photoexcited into the CB. In the second step, electrons are transported to the surface of the material where they experience some relaxation.[9]

When transporting electrons to the material surface, some are able to travel elastically without losing any kinetic energy. Whereas some loose most of their kinetic energy due to scattering but still have sufficient energy to barely overcome the material work function. Thus, becoming secondary electrons. The energies obtained in the UPS spectrum are plotted relative to the position of the E_F and consist of valence electrons, as well as secondary electrons.[91] This is the case for electrons getting emitted from a PEA surface just like in the case for Figure 23c.

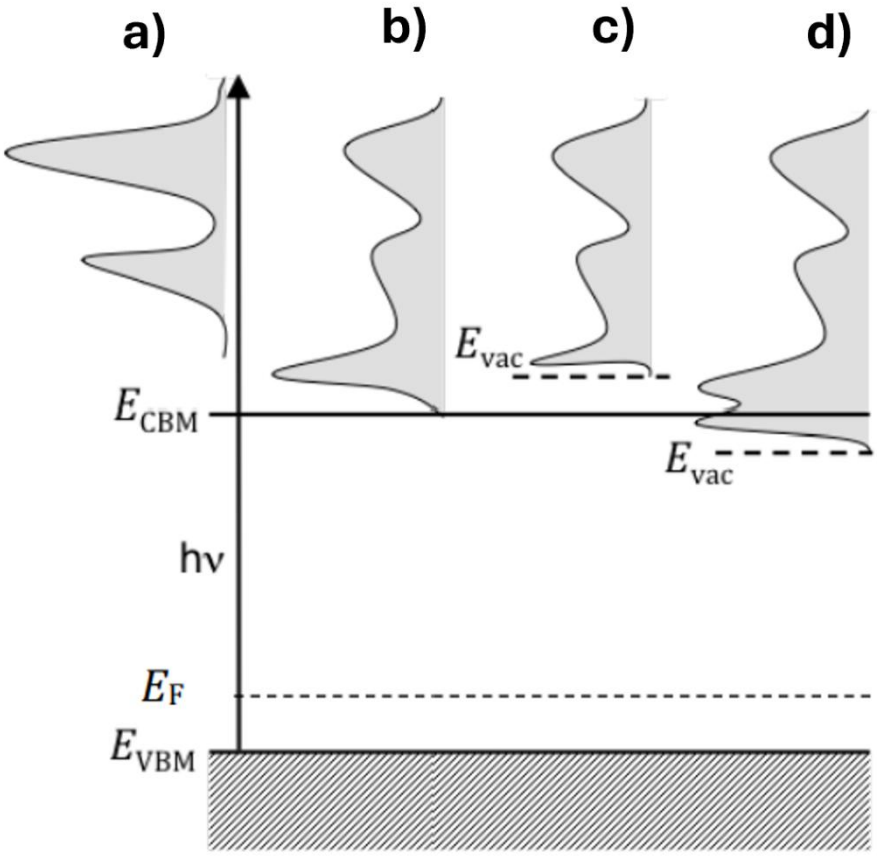

Figure 23 The successive steps depicting how a UPS spectrum is formed. a) Electrons getting excited from the VB into the CB. b) Electrons relaxing in the CB. c) PEA. d) NEA. This diagram was re-labelled from Ref. 9.

However, when electrons are emitted from an NEA material, they exhibit an additional high-intensity secondary electron peak at high binding energies. This is due to the CBM being pinned above the vacuum level, allowing for additional secondary electrons with energies higher than the vacuum level to get emitted.[9] In Figure 23d the additional secondary electron peak associated with the NEA has been shown.

For PEA materials the high-intensity onset characterised by the secondary electron cut-off (SECO), allows for the determination of the material work function. This relationship is shown in Equation 10 where the difference between the energy of the UV photon E_{UV} and SECO give the work function. [91,92]

$$\phi = E_{UV} - SECO \tag{10}$$

A picture and diagram of the UPS in the NanoESCA has been depicted in Figure 24. A monochromatic He (I) lamp supplied UV photons with an energy of 21.2 eV that was used for analysis. Electrons entered the double-hemisphere analyser, where the first hemisphere filtered the kinetic energies of electrons. Then, they were passed onto a channeltron where the signal got amplified before getting detected.

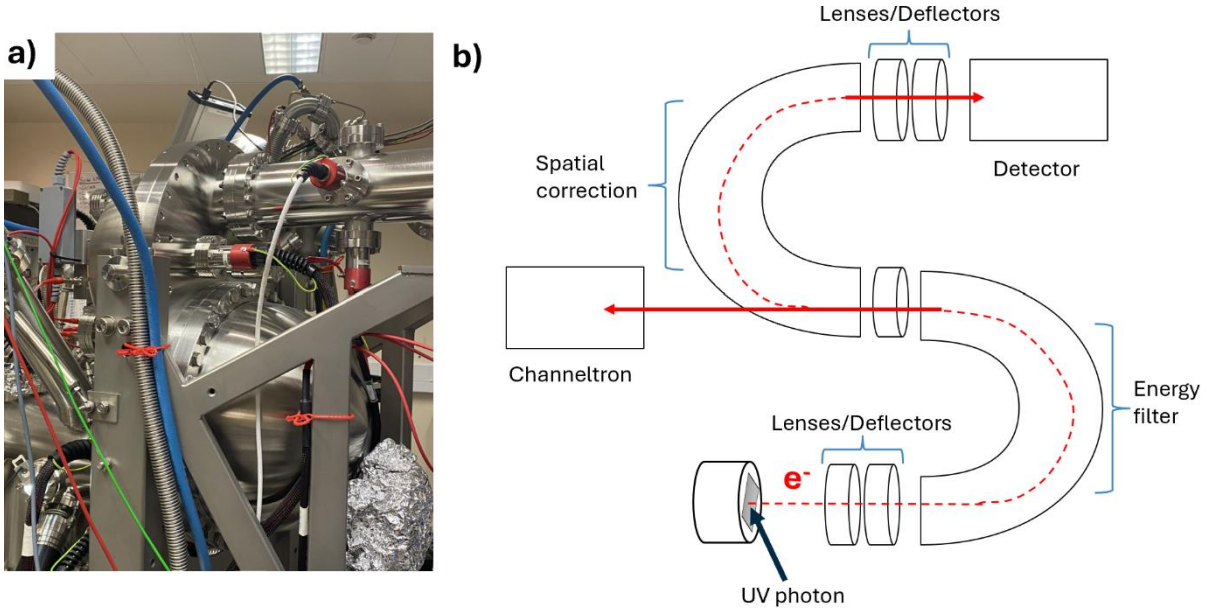

Figure 24 a) A picture of the UPS inside the NanoESCA. b) A diagram explaining the operation of an UPS created with reference to Ref. 9.

2.2.6 Energy Filtered Photoelectron Emission Microscopy

The EF-PEEM was used to create a 2D work function map over an area of the sample. To produce that, EF-PEEM used a nonmonochromatic Hg-vapor lamp with energies less than 5.8 eV for photoelectron emission. Measurements were taken in the same double-hemisphere analyser used for UPS, shown in Figure 24. However, this time after kinetic energy filtering, electrons moved onto the second hemisphere where they underwent spatial correction before getting detected. The field view value was adjusted to diameter of approximately 40 µm by iris tuning.

2.2.7 Scanning Electron Microscopy

The high-resolution images of the diamond surface morphology and the back gratings were produced using scanning electron microscopy (SEM). An SEM set-up has been illustrated in Figure 25. The electron gun supplied the instrument with electrons that can be accelerated to a specific accelerating voltage. With the help of condenser lenses the diameter of the electron beam was reduced, before arriving at the objective lenses which focused it onto the sample. The scanning coils on the objective lens allowed for

the x and y positions of the electron beam to be controlled. Once the beam struck the sample, secondary electrons were emitted and processed by a detector.[93]

A JEOL IT300 scanning electron microscope was used for SEM analysis. All images were taken from a top-down angle at 0°. Multiple pictures were taken with magnifications varying from x200 to x5500. For the back-grating images an accelerating voltage of 15 kV and working distance of 10.1 mm was used. Whereas an accelerating voltage of 25 kV and working distance of 10.6 mm was used the diamond morphology imaging. This set-up was put under high vacuum to ensure that high resolution images of the sample surface were obtained.

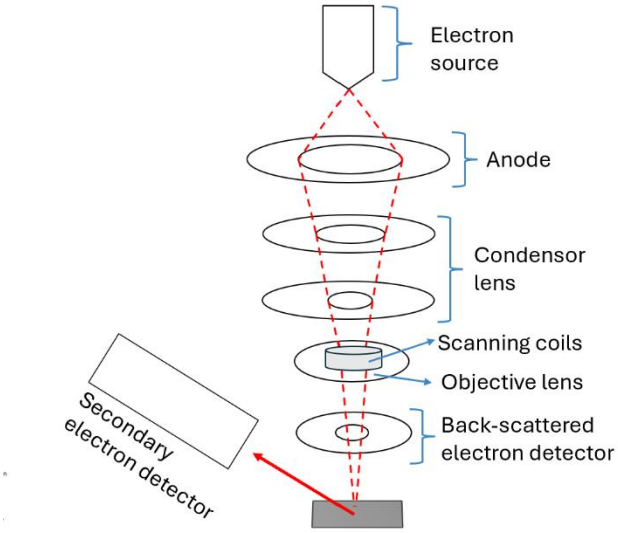

Figure 25 A diagram of the pathway taken by the electron beam during SEM measurements. This diagram was created with reference to Ref. 93.

2.3 LEXT Laser Microscope

An Olympus LEXT OLS5100 3D Measuring Laser Microscope was used to determine the thickness of the doped layers. This microscope was equipped with a 405 nm laser and had objectives from 10x to 100x magnifications. The LEXT was able to produce 3D surface acquisitions, from which height profiles could be generated with reference to the sample stage.

2.4 Laser cutter

The laser cutter was used to produce gratings on the back of the BNDL sample and to cut the 3x3 mm and 7x7 mm Ni-59 collectors as well as their holders to load them on

the TECsim. These were created by a laser micromachining system (Alpha 532, Oxford Lasers), with a diode-pumped nanosecond (Nd:YAG) laser.

A script that created gratings with a 10.5 μm separation was previously programmed using the ALPHACAM computer-aided design (CAD) software by Dr. Ramiz Zulkharnay. The script was transposed onto the Cimita v4.3.6 laser control software, which was connected to a servomotor allowing for the control of the x, y and z positions of the sample for cutting. Similarly, the square 3x3 mm and 7x7 mm Ni-59 collectors were cut. The holders of these collectors were designed and cut by Isaac Lui. The size of these Ni holders will be discussed with further detail in section 2.5.

2.5 Thermionic Energy Converter simulator (TECsim)

The TECsim is a homebuilt device found in the Bristol Diamond Lab. It was specially designed to measure the temperature and current generated by emitter samples when they were heated under vaccum.

As shown in Figure 26a, Sample 1 was placed on top of a circular quartz plate. This was used to isolate it from neighbouring currents and prevent heat transfer into the surroundings. Sample 1 was positioned in the centre of the quartz plate, such that the back of it covered a circular hole with a diameter of 8 mm. Two screw tightened Mo clips were used to secure into place. A W wire was connected to one of the Mo clips. This wire was then placed inside a W tube which allowed for an electrical bias to be applied onto the emitter.

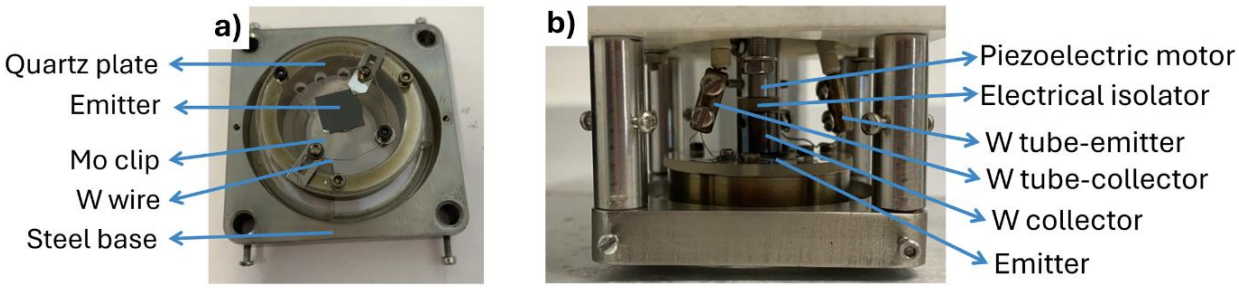

Figure 26 a) The set-up showing how the emitter was mounted on the quartz plate. b) The TEC configuration and wire assembly that allowed for a bias to be applied onto the emitter and collector.

The built-in cylindrical W collector of the TECsim with a diameter of 10 mm that was used to measure the emission current, has been shown in Figure 26b. The position of the W collector, therefore the interelectrode gap between both electrodes, was controlled by a piezoelectric motor (Z825BV, Thorlabs, Inc.) Similarly a W wire connected to the collector was placed inside a W tube to be able to apply a bias as well as measure the current generated.

Once sample mounting was completed, a voltmeter was used to check that the connector and emitter were not in contact. The set up was put under high vaccum. A preassure of ~1×10^{-8} torr was achieved by first using a rotary pump (Scrollvac SC30D), followed by a turbomolecular pump (Edwards EXT 75DX CF63).

An IR CO_2 laser (Firestar V40, SYNRAD Inc.) with a 40 W power output and wavelength of 10.5 µm was used to heat the sample. This was facilitated by passing the laser through a ZnSe window that had an anti-reflective coating of up to 12 µm (WG71050-G, Thorlabs, Inc.) and using three gold-coated copper mirrors to bend the beam upwards where it was focused onto the sample. The temperature of the sample was monitored using a two colour IR pyrometer (Spotmeter R160, Land Instruments International Ltd.). Unlike the diamond growth, the emissivitty was set to 0.10 due to an error in the pyrometer. The configuration of the TECsim has been depicted in Figure 27.

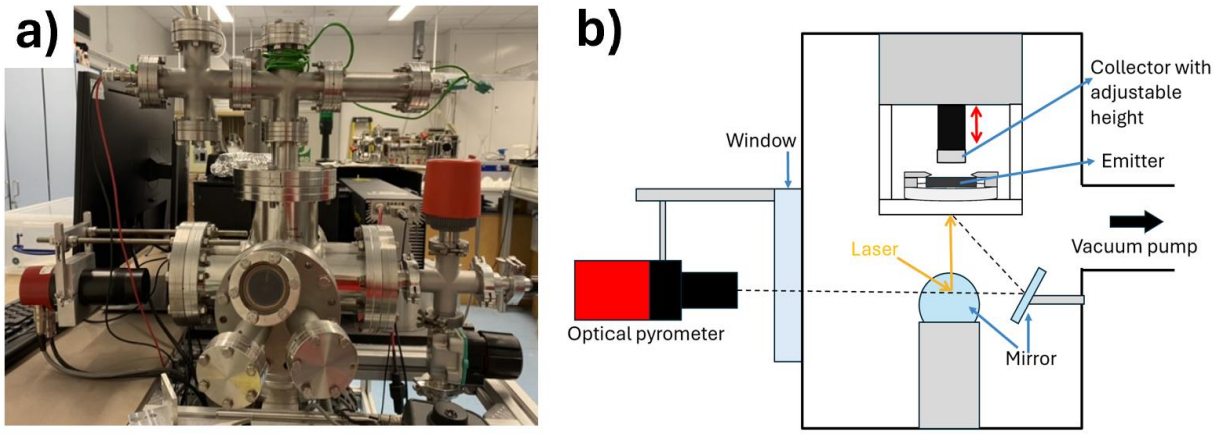

Figure 27 a) The TECsim found in the Bristol Diamond Lab. b) The operation of the TECsim which shows how the laser heated the emitter and how the pyrometer measured the temperature of the emitter. The height of the collector can be changed, to adjust the interelectrode gap. This diagram was created with reference to Ref. 82.

LabVIEW software allowed for the control of the laser output and the set-point temperature during heating cycles. The set-point temperature reading was stabilised through proportional integral derivative (PID) control. It was a trial and error process to determine the right values for each of the three parameters such that the maximum offset would be ± 2 °C. Therefore all temperature readings had an error value of ± 2 °C. For all runs, 0.500, 0.040 and 0.005 were chosen as PID values, respectvely because they satisfied these conditions.

Before strating the TEC tests, the samples had to be pre-heated to ensure that the emitter would not struggle with reaching high temperatures during data acquisition. This was called the “activation cycle” and involved heating the emitter from 300°C to 600°C in 50°C steps, where each step lasted for three minutes. Once 600°C was reached the sample was cooled down in a similar manner.

During all TEC tests, the emission current generated was masured by a current meter (Kiethley 2750 Multimeter/switch system). TEC tests were conducted on Sample 1

by programing a heating cycle from 300°C to 700°C with a ramp rate of 1°C per second. A one hundred second dwell time was added to the maximum temperature. After that, the temperature cycled back down to 300°C. The overall shape of the heating cycle resambled a trepazoid. From this data, the maximum emission current density (MECD) and threshold temperature, the temperature where electron emission was first observed, were analsed. This is the common approach used to analyse thermionic emission by the Bristol Diamond Lab. Instead of the Richardson-Dushman model to measure emission current densities because it assumes a uniform work function across the surface, which is rareley the case experimentally.[48] Since the MECD occurred at the highest temperature of 700°C, the error in the MECD was calculated by the standard error of the emission current density values produced at that temperature over one hundred seconds.

Finally, the Ni collector structure was different from that of the built-in W collector in the TECsim. The Ni collector was placed inside of a holder which was was attatced onto the W collector with the help of holding screws. The set up has been shown in Figure 28. The Ni holder consisted of three components: the capture, spacer and backplate. The capture carried the Ni collector and had a circular hole at the centre, to expose it to the emitter. This hole had a diametre of 1.2 times the length of the Ni collector, therefore the capture for the 7x7 mm Ni collector had a diameter of 8.4 mm and the 3x3 mm collector

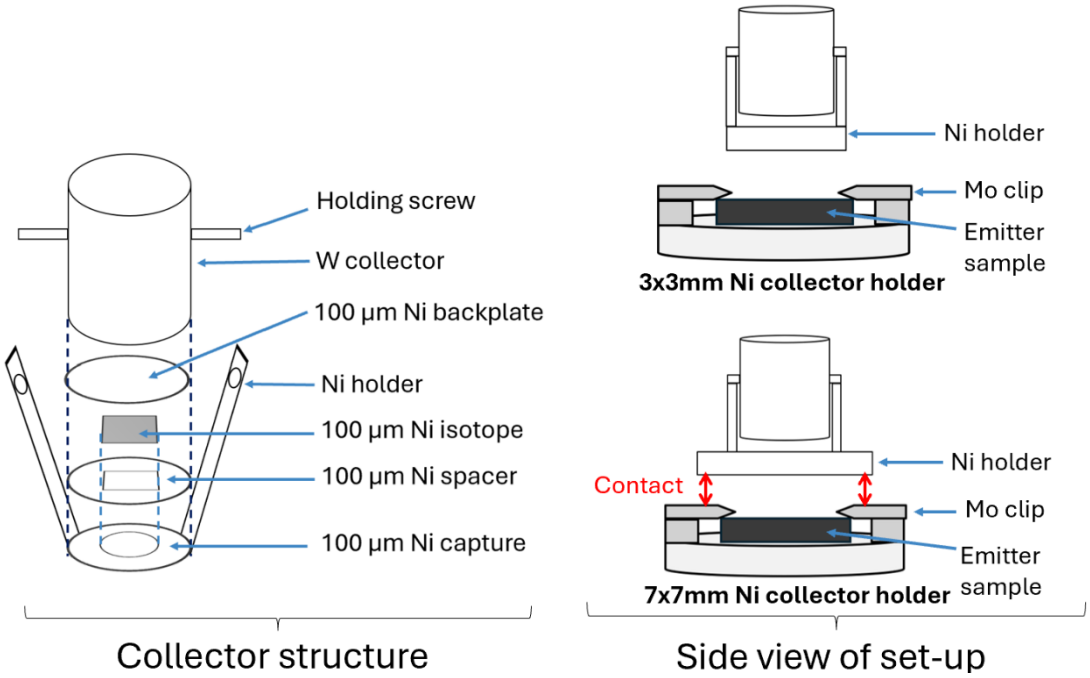

Figure 28 a) A diagram of how the Ni collectors were placed inside the Ni holder by a capture, spacer and back plate. The Ni holder is attached to the built-in collector of the TECsim by holding screws. b) Size comparisons of the 7x7mm Ni holder and the 3x3 mm Ni holder showing that the distance the 7x7 mm Ni cannot be lowered to the same extent as the 3x3 mm Ni due to contacting the emitter holder.

foil had a diametre of 3.6 mm. The spacer had a square hole in the middle of it, which had the same dimensions as the Ni collector because it was used to secure it into place.

Finally, the backplate covered the spacer which further prevented the Ni collector from falling off.

By looking at the side view of the 3x3 mm and 7x7 mm Ni isotope holders, it is clear that the 7x7mm holder was larger than the W collector it was attatched to. This has resulted in the interelectrode gap of the 7x7 mm Ni holder to be significantly higher than the 3x3 mm holder because it was in contact with the Mo clips that held the emitter. Unfortunately, the TECsim was not able to measure the exact interelectrode gap distance but the differences in interelectrode gaps were visible by eye.

3 Results and Discussion

3.1 The Structure of the Emitter

Height profiles of Sample 1 obtained from the LEXT, revealed that the BDL had a thickness of 23 µm and the NDL had a thickness of 1 µm. Thus, the total thickness of the Sample 1 was 524 µm. Sample 2 was assumed to have the same structure as Sample 1. This has been reflected in the rest of this section as well, where Sample 1 and 2 were assumed to be identical because they were produced under the same conditions.

3.2 Doping Effects on Raman Spectra

Raman spectroscopy was used to evaluate the effect doping had on the diamond structure. The intensities of the peaks in the spectra were normalised with respect to the sharp diamond peak that appears at approximately 1332 cm^{-1}, which was the peak with the highest intensity.[94] Furthermore, the green laser light used for analysis was about 50 times more sensitive towards sp^2 C than sp^3 C.[95] Which is why the graphite region of the spectrum that typically appears at approximately 1537.65 cm^{-1} was more intense by a factor of 50 than what it should be compared to diamond.[94,95] Even though this increased intensity made it falsely seem like graphite was very abundant, this allowed for detailed comparisons between the undoped TM100, BDL and NDL spectra.

In order to monitor how the diamond structure changed over the successive growth of doped layers, first the spectrum of the TM100 PCD diamond wafer was taken prior to doping as shown in Figure 29. These results from Figure 29 were expected since

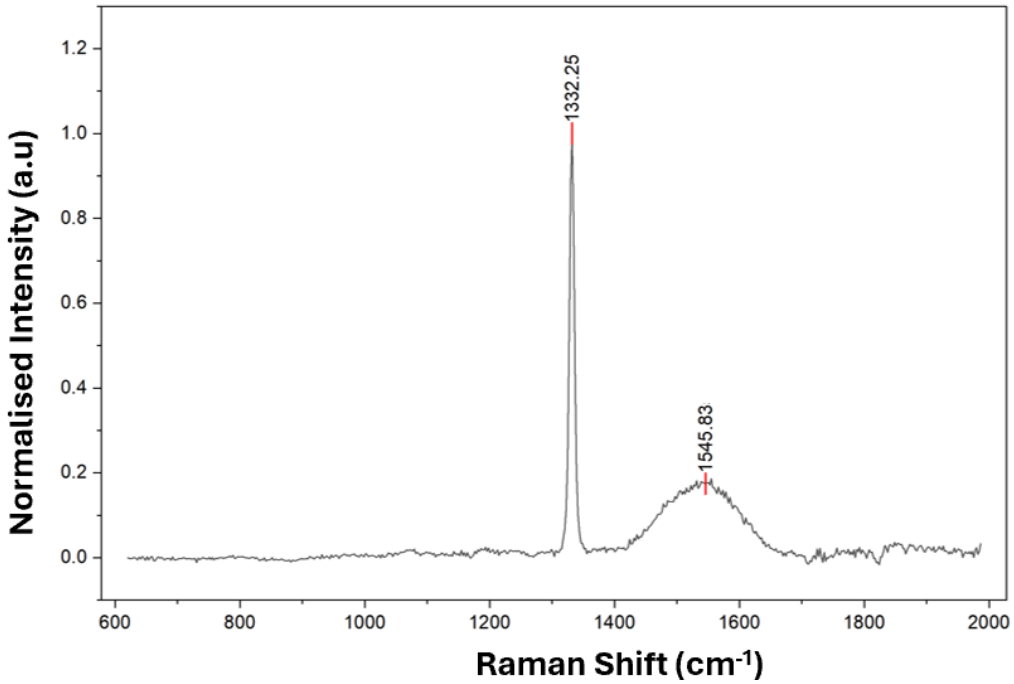

Figure 29 The Raman spectrum of the undoped TM100 diamond wafer. The peak at 1332.25 cm^{-1} corresponds to diamond and had a FWHM of 9.64 cm^{-1}. The peak at 1545.83 cm^{-1} corresponds to graphite.

the TM100 diamond wafer was polycrystalline, therefore consisted of graphitic grain boundaries which appeared at 1545.83 cm^{-1} alongside the diamond peak at 1332.25 cm^{-1}.

Figure 30 and Figure 31 show the Raman spectra of Sample 1 obtained from the stepwise growth of a BDL and a NDL on top of that, respectively.

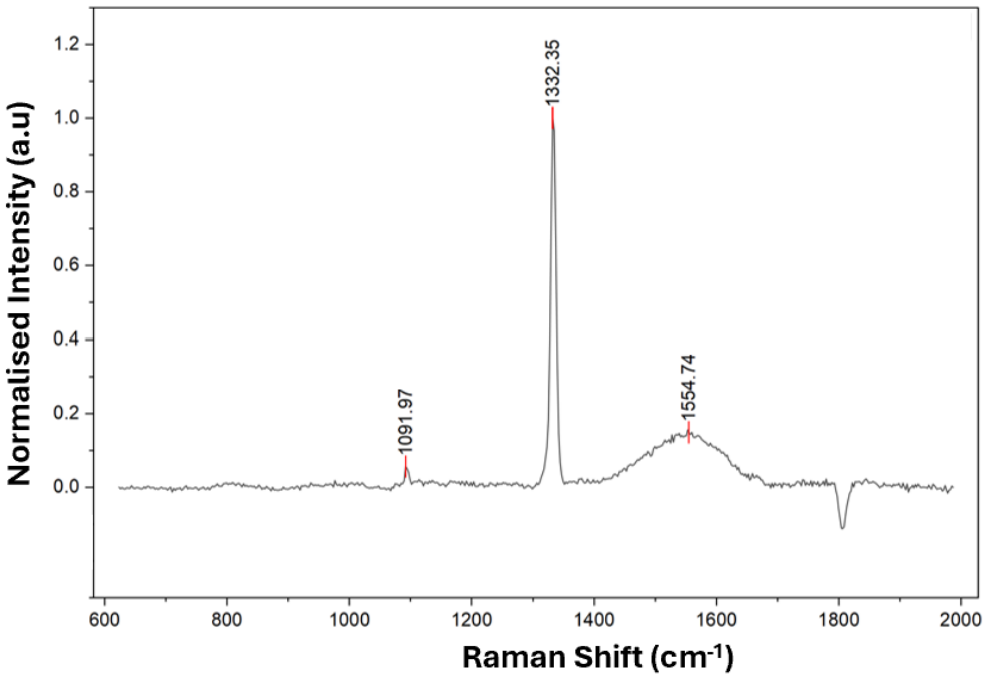

Figure 30 The Raman spectrum of the BDL grown on the TM100 wafer. The diamond peak at 1332.35 cm^{-1} had a FWHM of 10.23 cm^{-1}. The peak at 1091.97 cm^{-1} corresponds to TPA found in nanocrystalline grain boundaries and the peak at 1554.74 cm^{-1} corresponds to graphite.

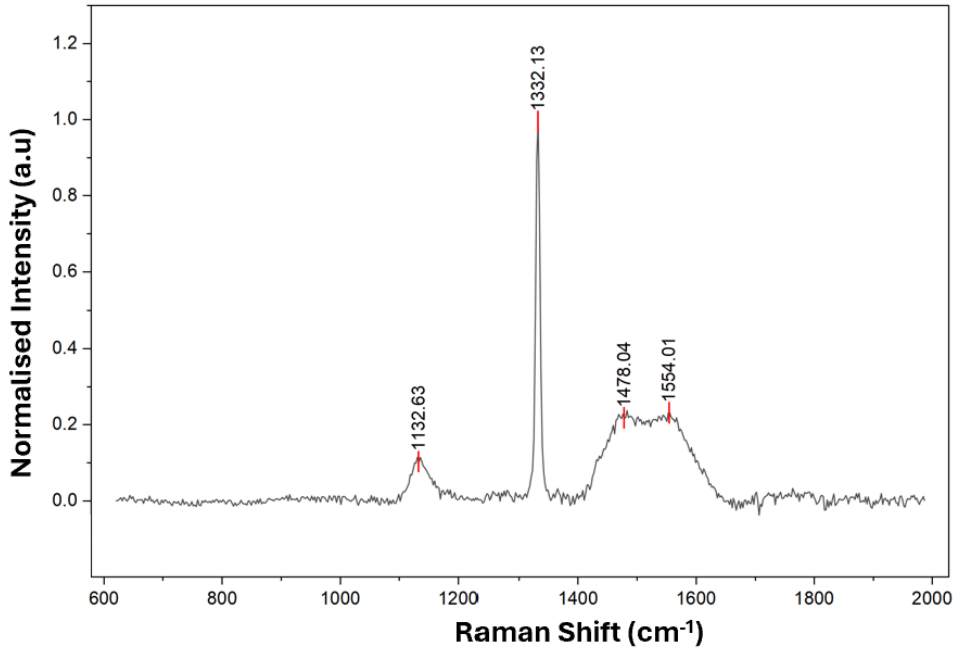

Figure 31 The Raman spectrum of the NDL grown on the BDL. The diamond peak at 1332.13 cm^{-1} had a FWHM of 9.36 cm^{-1}. Both peaks at 1132.63 cm^{-1} and 1478.04 cm^{-1} correspond to TPA in nanocrystalline grain boundaries. The peak at 1554.01 cm^{-1} corresponds to graphite.

The BDL spectrum might look similar to the TM100 spectrum because it also had diamond and graphite peaks occurring at 1332.25 cm^{-1} and 1554.74 cm^{-1}, respectively. However, an additional low-intensity peak at 1091.97 cm^{-1} was added. This may correspond to the presence of trans polyacetylene (TPA) at the grain boundaries of nanocrystalline diamond.[94] This peak is always accompanied by another TPA peak at approximately 1480 cm^{-1}. However, due to the low intensity of the 1091.97 cm^{-1} peak, the other peak might have also been low-intensity causing it to be a part of the background noise.[96]

Adding the NDL on top of the BDL, altered the diamond structure. From Figure 31 the most obvious difference was that both the graphite peak at 1554.01 cm^{-1} and the TPA peak at 1132.63 cm^{-1}, rose in intensity compared to the BDL. The TPA content was so high in the NDL that the second TPA peak also appeared at 1478.04 cm^{-1}.

Longer growths, such as the case for the BDL formation, have been previously reported to form large grain sizes which reduced the amount of graphitic grain boundaries.[97] This can explain why the graphitic peak in the NDL had a higher intensity than the BDL. Since the growth time of the NDL was six times shorter than the BDL, this could have caused more grain boundaries to form.

The quality of the doped layers grown were be assessed by the FWHM of the diamond peak. The broadening of the diamond peak is usually related to disorder in the diamond lattice, which translates to a higher FWHM.[98] Therefore, the FWHM was predicted to increase upon the addition of B since it has a larger covalent radius than C. This was observed when comparing the FWHM of the TM100 and the BDL that occurred at 9.64 cm^{-1} and 10.23 cm^{-1}, respectively. The FWHM of 9.36 cm^{-1} for the NDL, was lower than the undoped TM100. At first, this result may be unexpected because N distorts the diamond lattice due to preferentially forming a lone pair on itself when it is substitutionally bounded to C.[43] Instead, this increased order brought by the lower FWHM can be understood through how the incorporation of N changed the diamond orientations. Tsang *et al* found that in CVD diamond growth a plasma containing an additional 0.25% N_2, favoured the formation of (100) square facets.[99] The same could apply for Sample 1 and the order brought by forming more (100) orientated diamond could have lowered the FWHM slightly compared to the TM100 PCD wafer that had more randomly orientated diamond.

3.3 Determining Surface Elemental Composition by XPS

The findings obtained by Raman Spectroscopy were complimented by XPS, which was used to identify the elemental composition of the surface of Sample 2. The survey scan, with peaks corresponding to the bonding environments in Sample 2 over a wide binding energy range has been shown in Figure 32.

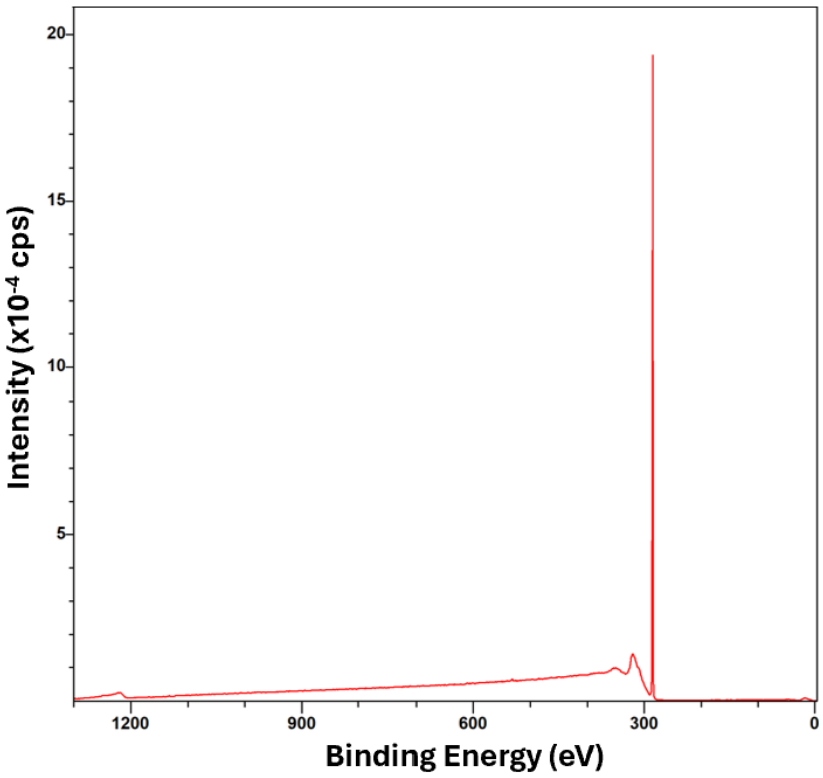

Figure 32 The XPS survey scan of Sample 2. The peak at 285 eV corresponds to the C 1s core level.

Only the C 1s peak appeared with high intensity in the survey scan. Since Sample 2 was transported to the NanoESCA inside a vessel filled with inert argon (Ar) gas directly after H-termination, a low intensity O 1s peak was observed in the O 1s high-resolution scan. This demonstrated that very little oxidation occurred at the surface terminating species which meant that the H-terminations, therefore the NEA of the sample was preserved during characterisation. The O 1s spectra has been given in Figure A1 in the appendix.

The high-resolution XPS spectrum of the C 1s peak has been shown in Figure 33. The bright red curve is the experimental curve and additional peaks were fitted into it according to the chemical species present. Since the B 1s and N 1s peaks were not detected in the survey scan nor in their individual scans, the C-N or the C-B chemical environments have not been fitted to the C 1s peak. The O 1s was also not fitted due to its low intensity that would not significantly contribute to the peak fitting. Therefore, only the sp^3 diamond and sp^2 graphite peaks were fitted. The grey curve that shows the combination of these fittings was not visible in this spectrum. Thus, it was effectively overlapping with the bright red experimental peak and indicating that peak fittings were accurately carried out. The diamond and graphite peaks occurred at 285.47 eV and 286.21 eV, respectively.

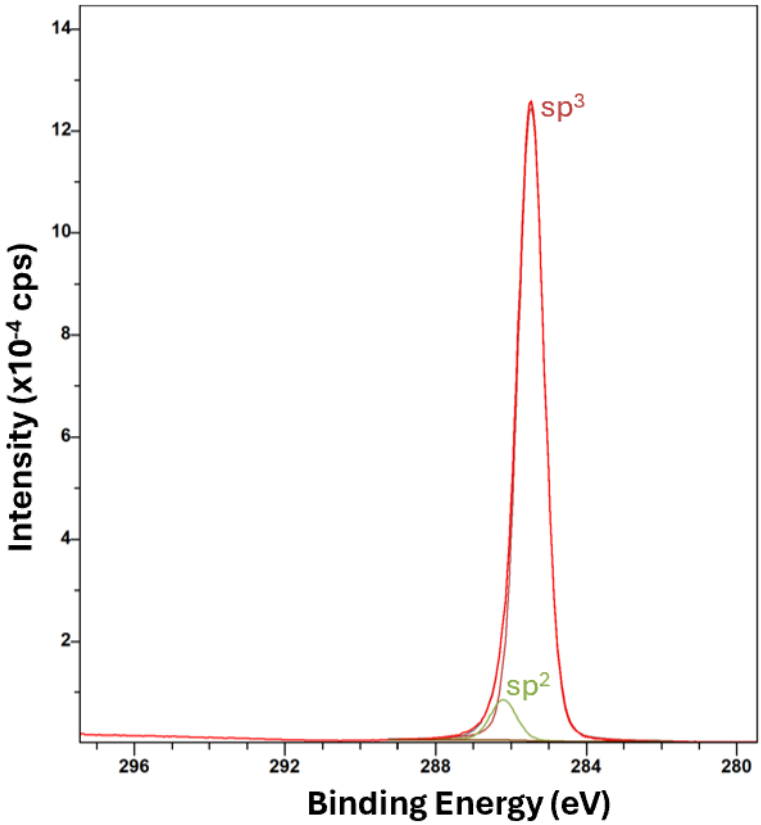

Figure 33 The diamond and graphite peaks at 285.47 eV and 286.21 eV, respectively.

Similar to the survey scan, no B 1s nor N 1s peaks were observed in the high-resolution scan either. Since XPS is surface sensitive with a resolution up to 10 nm, the BDL buried under the 1 µm NDL was undetected. One possible reason for the absence of N 1s in the XPS spectrum can be attributed to the N content in the NDL being below the XPS detection limit. In previous experiments with NDD, the detection limit of N in XPS was determined to be at an atomic percent of 0.5%, which is described as the number of atoms of a specific element with respect to the total number of atoms in an area. This atomic percent corresponded to a N concentration of 8.5×10^{20} cm^{-3}.[100] It is likely that the concentration of N was low in the NDL of Sample 2 because not only was the growth time as short as 15 minutes, but also during H-termination the H_2 plasma could have etched some of the NDL which further decreased the N content.[101] For example, measuring the N concentration of Sample 2 through secondary ion mass spectroscopy (SIMS) and comparing the concentration of N in the sample to the detection limit of 8.5×10^{20} cm^{-3}, can conclude whether the N content fell below the XPS detection limit. Another reason for the absence of the N 1s peak could be due to operational errors such as mounting the wrong side of the sample, the TM100 undoped diamond face, for analysis.

3.4 Determining the NEA by UPS

The work function, VBM position and electron affinity values of Sample 2 could have been calculated using UPS. However, Sample 2 was charging during UPS measurements. This meant that the sample was not conductive enough to compensate for the electrons lost in photoemission as a positive charge accumulated on the surface. This effect was irreversible and led to the energy values read on the graph to get offset by a small unknown amount. So, the work function, VBM position and electron affinity can only be estimated from UPS spectrum.[102] The UPS spectrum of Sample 2 has been given in Figure 34.

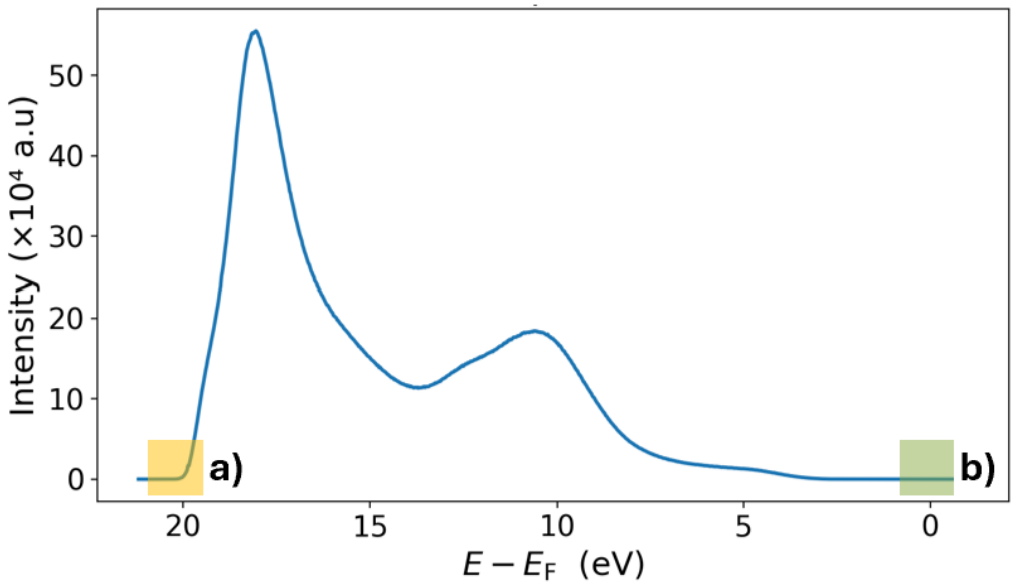

Figure 34 The UPS spectrum of Sample 2 where the yellow region corresponds to the CB state whereas the green region corresponds to the VB state.

The highlighted yellow and green areas correspond to areas where the SECO and VBM energy values can be approximated, respectively. Due to the significance of these areas, they have been zoomed in Figure 35 for further investigation.

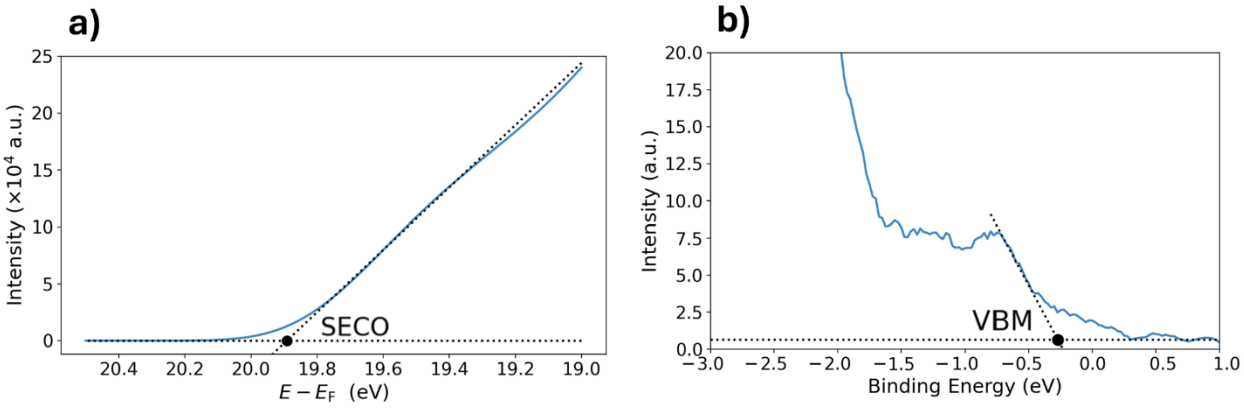

Figure 35 Zoomed in regions of the UPS spectrum. a) Determining the SECO from the CB region of the spectrum. b) Determining the VBM from the VB region of the spectrum.

The linear extrapolation method was used to calculate the VBM position of Sample 2 in Figure 35b. This was found to be 0.27 eV below the E_F. Due to charging, there is little confidence in this value. Previous work by Zulkharnay further proved that this value for the VBM position is wrong due to charging. He has found that the VBM positions given by UPS for (100) and (111)-oriented H-terminated SCD were 0.72 eV and 0.89 eV, respectively.[103] Even though Sample 1 was a PCD sample, this high energy difference suggested that significant charging occurred.

If the exact value of the VBM were to be calculated, in an experiment where no charging was observed, the electron affinity of the sample could have also been calculated using Equation 11. Where E_g is the known band gap of the material, in this case diamond with 5.57 eV. An NEA is obtained if the result has a negative sign.

$$\chi = \phi + (E_F - E_{VBM}) - E_g \tag{11}$$

Even though the NEA cannot be quantitatively calculated for Sample 2, the UPS spectrum still provides qualitative information that supports the existence of a NEA. As previously explained in section 2.2.5, when the vacuum level is below the CBM an additional secondary electron peak forms that is indicative of an NEA. Work by Torrengo proves this phenomenon by studying the effect of inducing a PEA onto NEA surfaces through the successive oxidation of undoped nanocrystalline H-terminated CVD diamond films. They showed that as oxidation increased, the surface that once had NEA properties transitioned to a PEA surface. This change was monitored through UPS, which showed a drastic decline in the secondary electron peak.[104] Based off that research, the spectrum in Figure 34 does show the characteristic high-intensity peak of an NEA at high binding energies.

Another consequence of having a NEA surface is that the work function cannot be exactly determined. Even if the sample was not charging, the extra secondary electron peak complicates the determination of the SECO, therefore the work function. Which is why the previously shown Equation 10 can only be used to determine the work function of PEA surfaces.[103]

3.5 EF-PEEM Work Function Map

Due to the issues associated with determining the work function by UPS, EF-PEEM was used because it is a more powerful tool. Not only does EF-PEEM measure the material work function, but it produces a work function map across an area. Sample 2 was also charging during EF-PEEM experiments which meant that, once again, the work function values obtained by EF-PEEM were offset by an unknown amount. Instead of

analysing work function values, the work function map in Figure 36 was used to observe the variability of the work function over the diamond surface.

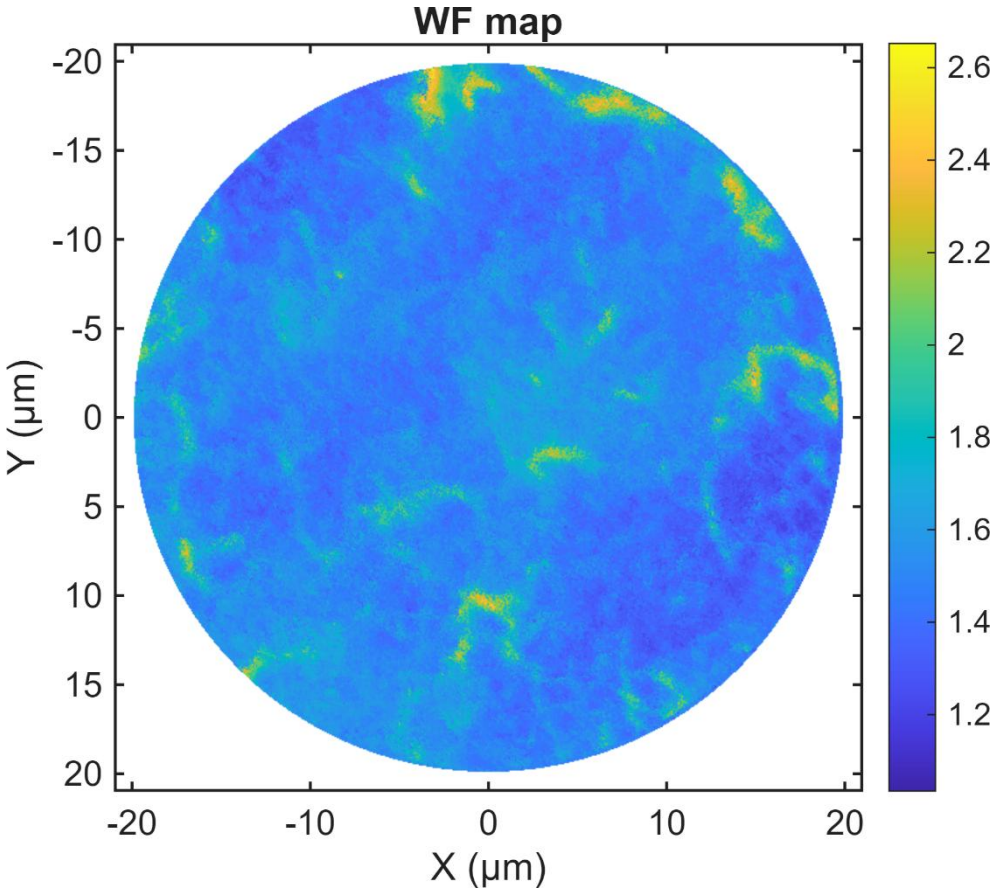

Figure 36 The work function map of an area in Sample 2 with a diameter of 40 µm. The colour gradient to the right shows the work function range in this area.

The EF-PEEM map has demonstrated the consequence of having diamond grains and grain boundaries in PCD samples because the work function changed across the surface. The yellow and bright green lines on the map correspond to grain boundaries which had a work function between 2.6-1.8 eV, which was higher than diamond. Furthermore, the different diamond grains also did not have consistent work function values due to having different orientations which varied across 1.6-1.2 eV. This is evident because the EF-PEEM image showed separate regions where different shades of blue dominated, rather than a continuous colour that would indicate work function uniformity. As a result, in TEC tests it was expected that different areas of the surface contributed to the emission current density differently.

3.6 Diamond Morphology and Back Grating Imaging

Using SEM, the morphology of the diamond grains and the grain boundaries separating them was imaged. Figure 37a and 37b show the surface of Sample 2 with

lower and higher magnifications, respectively. In both images it can be seen how no particular diamond orientation was prominent, therefore it was absent of an overall order. This is a characteristic of PCD films because they consist of diamonds with random orientations. In Figure 37b the grain boundaries separating the diamond grains can be seen in greater detail.

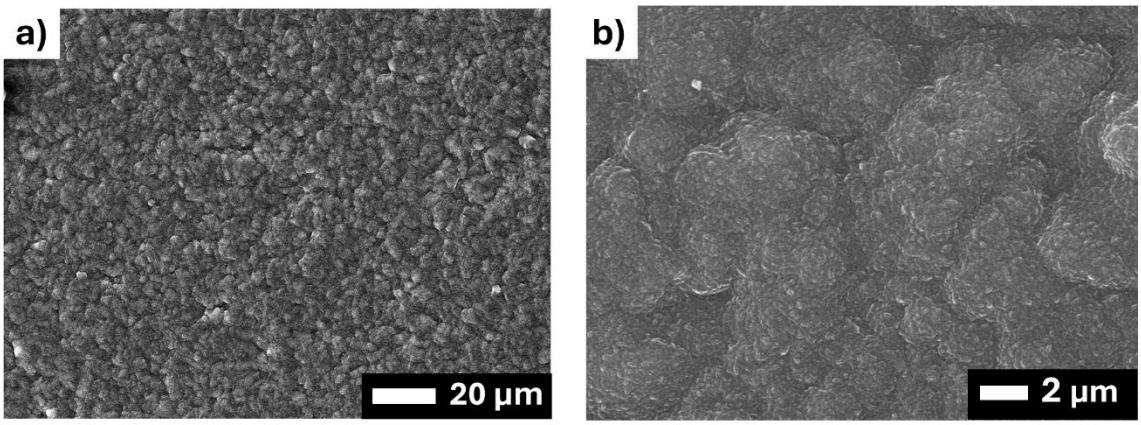

Figure 37 a) The surface of Sample 2 analysed with a x700 magnification and an accelerating voltage of 25 kV. b) The surface of Sample 2 analysed with a x1300 magnification and an accelerating voltage of 25 kV. Both images were taken by Dr Subash Sharma.

This absence of uniformity in PCD is significant because, as it was discussed in the work function imaging using EF-PEEM, the grain boundaries have different electronic properties than the diamond structure. Furthermore, each diamond orientation also has distinct electronic properties.

Maximising laser absorption to the emitter was key to allow for it to be effectively heated and release more electrons. Therefore, grating patterns with a gap matching the IR laser wavelength,10.5 µm, were produced at the undoped face of Sample 1.[72] The quality of the back-gratings of Sample 1 were imaged prior to TEC testing to check that they were not damaged during laser cutting and appear as periodic straight lines. Figure 38 shows that the structural integrity of the straight lines was preserved.

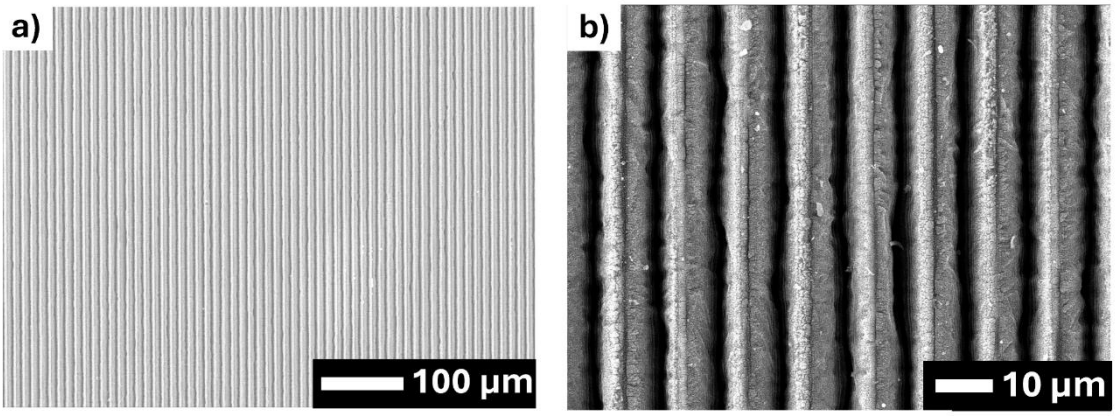

Figure 38 a) The back-gratings of Sample 1 analysed with a x400 magnification and an accelerating voltage of 15 kV. b) The back-gratings of Sample 1 analysed with a x1400 magnification and an accelerating voltage of 15 kV. Both images were taken by Dr Ramiz Zulkharnay.

3.7 Comparing Heating Cycles Across TEC Tests

TEC tests were run using Sample 1 as the emitter with W, 7x7 mm Ni-63, 3x3 mm Ni-59 and 3x3 mm Ni-63 as the collector. The built-in W collector was used as a preliminary TEC test before installing the Ni holders. Figure 39 shows an example profile of one heating cycle for both the 3x3 mm Ni-59 collector and the 3x3 mm Ni-63 collector, where the emission current density and temperature changed overtime. Since Sample 1 was heated from 300°C to 700°C, it was expected that the emission current density would rise with increasing temperature. This is because electrons would gain energy upon heating, which would allow for more of them to be excited to the CB and get emitted without a significant barrier due to the NEA detected by UPS.

From the example heating profiles Figure 39 it is evident that electron emission was detected at both 3x3 mm Ni-59 and Ni-63 collectors. This is because as the red temperature line rose, so did the black emission current density line. Thus, the emission current densities were temperature limited. The reason why the Ni-59 heating profile has a different shape from the Ni-63 is due to having a higher emission threshold temperature, which will be further discussed. Higher temperatures could have been tested to generate higher currents, but due to H desorption that occurs at temperatures higher than 700°C, this would come at the consequence of losing the NEA induced by H-termination significantly.[77]

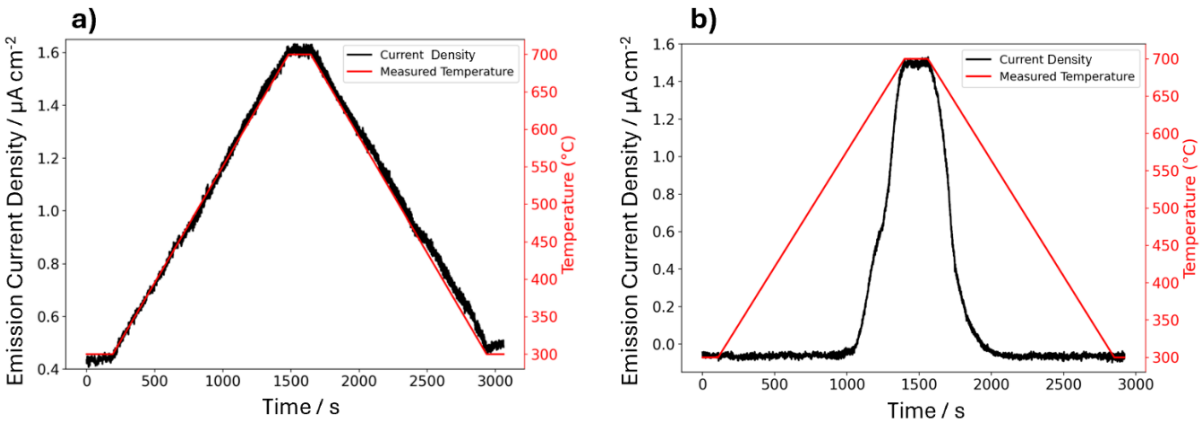

Figure 39 In both heating cycles the red curve showed the measured temperature and the black curve corresponded to the current density produced. a) An example heating cycle from the 3x3 mm Ni-63 TEC test. b) An example heating cycle from the 3x3 mm Ni-59 TEC test.

The only TEC test that did not follow the temperature dependent emission current density rise was observed with the 7x7 mm Ni-63 collector. This was a shocking result because even the non-beta enhanced TEC test with the W collector had produced emission prior to using the 7x7 mm Ni-63 collector. This issue lies in the wide design of the 7x7 mm Ni-63 collector holder, which limited how small the interelectrode gap could be because it contacted the Mo clips attached to the emitter. This was previously visualised in Figure 28. Due to the higher interelectrode gap, the emission current density decreased. This was expected because a wider interelectrode gap allows for more room to accumulate space charge as discussed in section 1.1.2. Since no emission was

observed across 3 trial cycles with the 7x7 mm Ni-63 collector, no further control experiments were conducted with a 7x7 mm Ni-59 sample. Instead, to produce a smaller interelectrode gap, a narrower collector was designed to hold 3x3 mm Ni-59 and Ni-63.

3.8 Ni-59 TEC Tests

The TEC test with 3x3 mm Ni-59 as the collector generated emission current that was temperature limited. Even though the exact value of the NEA or work function could not be determined, this test demonstrated that the electronic properties of Sample 1 were sufficient to enable electron emission without beta enhancement. The MECD and threshold temperature obtained across all heating cycles for the Ni-59 TEC, test has been plotted in Figure 40.

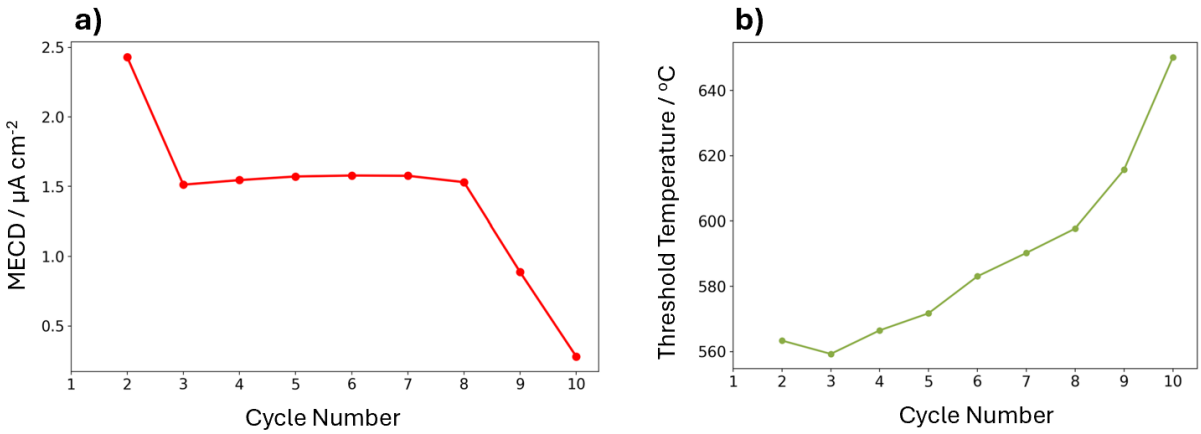

Figure 40 a) The MECD of the Ni-59 TEC test, across a total of nine heating cycles. b) The threshold temperature of the Ni-59 test that increased overtime across nine heating cycles. Since the standard error associated with the MECD measurements was to the order of 10^{-2} μA cm^{-2}, no error bars were plotted due to how low the error was. The ±2°C error of the temperature was also too small to scale in the graph.

As expected, across all heating cycles the MECD was consistently observed at the at the highest temperature, 700°C. The emission current densities produced during the one hundred-second dwell at that temperature, experienced small changes and allowed the MECD values to have a low standard error. Out of the ten cycles shown in Figure 40 only the first one produced no emission, which is why it was omitted. Going from cycle 2 to 3, the MECD dropped significantly from 2.43 ± 0.07 μA cm^{-2} to 1.51 ± 0.04 μA cm^{-2} due to H desorption.

Cycles 3 to 7 remained relatively stable with a very subtle increase in emission current density. The H_2 plasma may allow some H to escape into the diamond lattice and grain boundaries, during H-termination.[97] The presence of large amounts of graphitic grain boundaries in the NDL were previously confirmed by Raman spectroscopy, shown in Figure 31. On heating the emitter as part of the TEC tests, it is possible that some of the H in the diamond bulk re-generated onto the surface and formed a bond to the surface

C, preserving the H-termination. Thus, explaining why the MECD increased slightly overtime as Sample 1 was heated.

The re-generated H-terminations did not last long since, they also experienced H-desorption eventually. This was clear when looking at the steep decline in MECD going from cycle 8 to 10. More heating cycles could have been preformed to observe when all of the H-termination sites desorbed as the MECD approached 0.

Figure 40b, which shows the change in emission threshold temperature, supports the findings from Figure 40a. Generally, as more H desorbed from the emitter, the NEA started to transition towards a PEA. This is evident in Figure 40b because after each heating cycle, higher temperatures were required to release electrons from the CBM into the higher-lying vacuum level. The threshold temperature had the lowest value of 563 ± 2°C in cycle 2 and increased by 15% between cycle 2 and 10.

The same phenomenon was observed in the preliminary TEC tests with the W collector, shown in Figure 41. Similar to the Ni-59 collector, the W collector also showed an initial drop in MECD, followed by a subtle increase. However, not enough heating cycles were preformed to observed when the MECD dropped due to the desorption of re-terminated H. Since both non-beta enhanced Ni-59 and W collector TEC tests showed a similar trend over 10 heating cycles, the H re-termination argument is likely to be true and more experiments are needed to understand the detailed mechanism behind these observations.

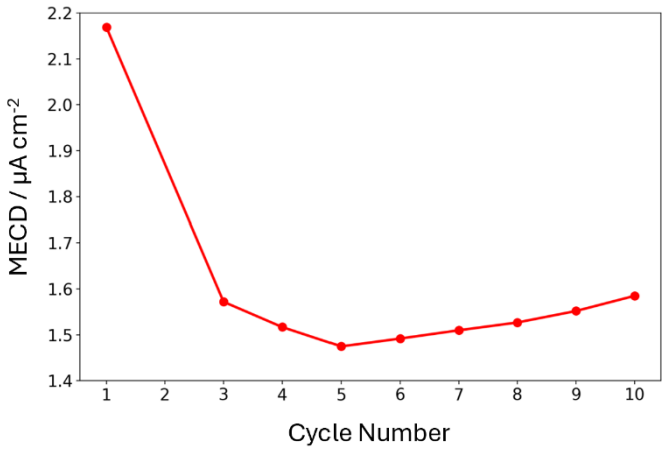

Figure 41 The MECD of the W TEC test, across a total of ten heating cycles.

3.9 Ni-63 TEC Tests

On the other hand, when the 3x3 mm Ni-63 collector was used for beta enhanced TEC tests, no data on the threshold temperature was obtained. This is because emission was consistently observed at the starting temperature of 300°C and even when lower starting temperatures were set, the pyrometer failed to accurately measure temperatures below 300°C. Therefore, the exact threshold temperature of Ni-63 is unknown, but it is

below 300°C. This threshold temperature was the lowest recorded among other beta enhancement experiments previously conducted in the Bristol Diamond Group, where beta enhanced threshold temperatures were typically observed at 500°C.[82,84] This low threshold temperature observed could be due to beta enhancement. As high energy electrons from the Ni-63 collector struck Sample 1 and skewed the Fermi-Dirac distribution, electrons with high kinetic energies were released at lower temperatures and hindered the formation of a space charge. Thus, emission was observed at temperatures lower than 300°C.

Figure 42 shows the MECD obtained at 700°C across all ten heating cycles for the 3x3 mm Ni-63 collector. One striking difference between the previous MECD plot of the Ni-59 test, was that the MECD of Ni-63 increased exponentially with each successive heating cycle. This was also not observed in previous work conducted by the Bristol Diamond Group. In Go's research on beta enhancement it was observed that the Ni-63 run involved an initial decrease in emission current due to H-desorption, just like in the Ni-59 run of this experiment. He called his findings beta enhanced because the emission current of the Ni-63 collector stabilised at higher emission currents than Ni-59 as previously shown in Figure 15.[82]

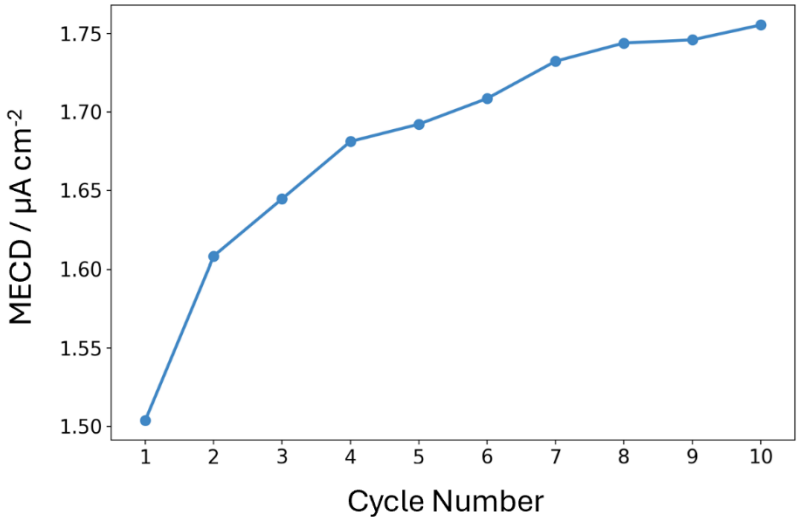

Figure 42 The MECD of the Ni-63 TEC test, across a total of ten heating cycles. The MECD increased exponentially across the heating cycles.

In the case of this experiment, the rise in MECD due to beta enhancement can be rationalised by the re-termination of H. In the case for the exponentially rising MECD across the heating cycles, H re-termination effects dominate the previously explained Fermi-Dirac distortion effects because the latter does not explain why the NEA and H-terminations were not lost overtime. It is possible that the H re-termination previously observed in the Ni-59 test, occurred more pronouncedly when the emitter was exposed to beta particles. This could be due to the high energy electrons released by the Ni-63 collector possibly forcing the H atoms to escape the grain boundaries and interstitial

sites for re-termination. The highest MECD value was obtained at cycle 10 with a value of 1.75 ± 0.02 μA cm^{-2}.

By the time Ni-63 was tested, Sample 1 was used in three different TEC tests meaning that it had previously undergone three H-terminations. Between each H-termination, it was expected that some of the surface diamond got etched due to using a H_2 plasma which is very effective at etching diamond.[101] As a result, the morphology of the diamond grain orientations and grain boundaries could have been altered. It is plausible that more grain boundaries were present in Sample 1 during the 3x3 mm Ni-63 test, since it was the last TEC experiment. As a result of that, more H could have accumulated within the grain boundaries before getting forced out by beta particles. So, both beta particle impact and H_2 plasma exposure had a significant effect on the plot observed in Figure 42.

3.10 Enhancement Factor

The effect of etching the surface became important when comparing the MECDs obtained at the start of each heating cycle for the 3x3 mm Ni-59 and Ni-63 tests, as shown in Figure 43a. Cycle 2 in Ni-59 had a MECD of 2.43 ± 0.07 μA cm^{-2}. It should be noted that if cycle 1 had worked for this collector, it would have been expected that the current would be even higher than cycle 2. Whereas the MECD in cycle 2 of Ni-63 occurred at 1.64 ± 0.01 μA cm^{-2}. The lower initial MECD of the Ni-63 collector could be attributed to H_2 plasma etching, once more. Since Sample 1 was exposed to more H_2 plasma before the Ni-63 test, compared to the Ni-59 test, it is also possible that etching disturbed the diamond surface such that less H-terminations were able to be formed on Sample 1 during the Ni-63 test.

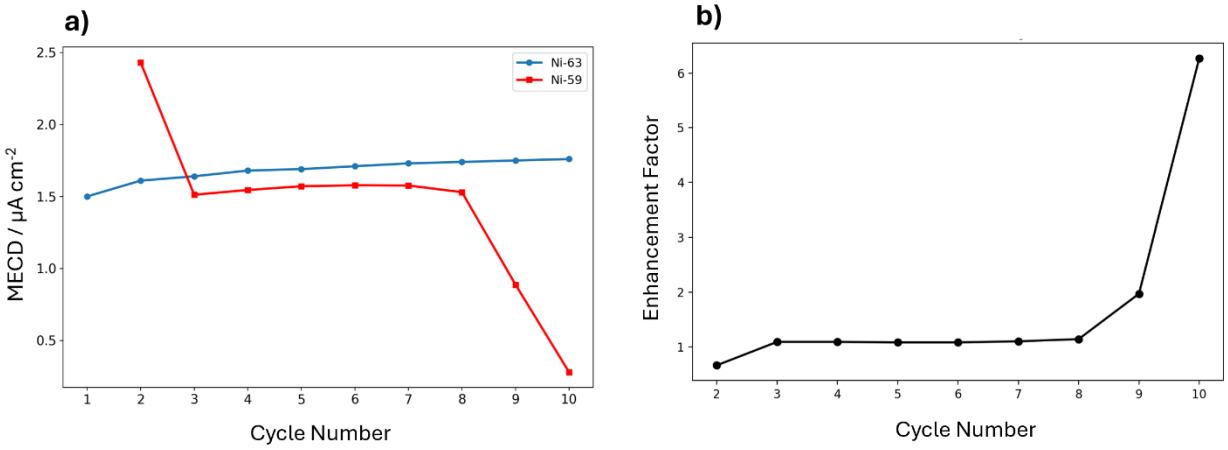

Figure 43 a) Overlaying the MECD graphs of the 3x3 mm Ni-59 and Ni-63 TEC test to compare their behaviour. b) The enhancement factor observed between cycle 2 and 10 for the 3x3 mm Ni-59 and Ni-63 experiments.

However, the higher MECD of the Ni-59 test was only the case for cycle 2. After that, all of the remaining cycles had higher MECDs for the Ni-63 test. Based off the ratio

of MECDs between the beta enhanced to non-beta enhanced runs, an enhancement factor across all cycles was plotted in Figure 43b. Before the H re-termination desorbed at cycle 8 for the Ni-59 test, the enhancement factor remained stable as low as approximately 1.09 across 6 cycles. Once the H desorbed and the MECD in Ni-59 dropped after cycle 8, only then were higher enhancement factors of 1.97 and 6.27 achieved for cycles 9 and 10, respectively. This enhancement factor is 43% higher than the enhancement factor obtained by Go et al which was 2.7.[82] From these values it can be deduced that the effects of beta enhancement appear in the long-term after completing 8 heating cycles. Therefore, with further development, an emitter similar to Sample 1 might be suitable for beta enhanced TEC applications where long operational lifetimes are needed.

It should be highlighted that in order to make a more conclusive remark on long-term beta enhancement effects, more cycles are needed to observe if beta-enhancement still shows an exponential enhancement for even longer operational periods such as 30 heating cycles and if they remain stable when exposed to 700°C for longer time periods. But based off the results provided in these experiments so far, it was observed that for longer TEC operational times beta enhancement through Ni-63 is key in minimising H-desorption and maintaining the NEA. Despite emission being observed with the non-beta enhanced Ni-59 collector, the loss of H does not make it desirable in the long-run.

4 Future Work

4.1 Repeating NanoESCA Measurements

Charging is a significant issue that must be prevented in future experiments in order to measure the exact work function and NEA of emitter samples. These parameters are important, especially in TEC applications, because they provide valuable information on the emission behaviour of electrons and can help rationalise the emission current density values obtained by experiments. When a sample charges in XPS, typically a low-energy electron flood gun is used to compensate for the positive charge build up on the surface. This is done with a calibration peak to measure the exact shift in the spectrum. Unlike XPS, in UPS due to the small binding energy range there are no good peaks that can be used for calibration. Instead, for a sample to be analysed under UPS it has to be made thinner in order to reduce resistivity.[105] Therefore, in future work Sample 2 can be recreated on a thinner TM100 wafer that is 0.3 mm thick (Product code: 145-500-0536) and supplied by Element Six. Alternatively, the doping ratios can be adjusted to produce a sample with better conductivity.

Furthermore, XPS measurements on Sample 2 need to be repeated to overcome the possible detection limit or the operational errors in order to obtain a N 1s peak.

4.2 Perfecting the Structure of the Diamond Emitter

Work due to be published by Isaac Lui in the Bristol Diamond Lab has studied a similar BNDL emitter structure used in this study. The only difference was that he grew the NDL for 30 minutes. However, his emitter sample showed no emission after H-termination. This is to be contrasted with this study, where the NDL was grown for 15 minutes. From this comparison it is clear that the emission properties of the BNDL samples change dramatically with N doping concentrations. Therefore, a more in-depth study involving multiple BNDL samples with different N and B doping ratios can be get carried out to understand this trend, thereby improving the emitter design for TECs. The data analysis of these experiments can draw inspiration from the work of Liu's group that used SIMS to accurately measure the B and N doping ratios, as well as Hall measurements to identify n-type character.[71]

Similarly, in an experiment with multiple samples, further experimental evidence of H re-termination due to resurfacing from the grain boundaries can be studied. BNDL samples with varying grain boundaries can be produced by changing the plasma conditions the MWCVD reactor. The morphology of the grain boundaries can be analysed in the SEM and the TEC tests of these H-terminated samples can be compared to see if grain boundary size has a significant effect.

4.3 Stable Surface Terminations on the Emitter

The major factor preventing stable MECDs and threshold temperatures from being obtained across all of the heating cycles in the Ni-59 TEC tests, was H desorption from the H-terminated Sample 1. To further improve this experiment, emitter samples can get terminated by thermally stable O-M terminations. Previous TEC experiments by Pearce reported that the OSc termination experienced little desorption even when heated up to ~850^{o}C and generated a current of 2.57 mA.[106] As discussed in section 1.5.2, LiO terminations can also be tested in future work due to their low NEA of -2.1 eV. Thus, O-M terminations should be able to provide high emission currents due to the higher surface dipole and thermal stability at elevated temperatures. Using O-M terminations in beta enhanced experiments could unveil new enhancement mechanisms beyond H re-termination and possibly increase enhancement factors further.

4.4 Improving the TECsim

The difference in interelectrode gaps across the 7x7 mm and 3x3 mm collectors played a major role in whether electron emission was detected. However, the only way to

understand the relative interelectrode distances was by eye. Therefore, the design of the TECsim could benefit from a system that precisely measured the interelectrode distance. This system could be produced by installing a laser displacement sensor to accurately measure the distance between the emitter and the collector.[107]

4.5 Developing Low Work Function Collectors

Producing a low work function collector is key to have a large work function difference between the emitter and collector to increase output power in a TEC. The Ni collector tested in this study had a work function of 5.15 eV, which was even higher than the emitter.[108] To achieve maximum output power in a TEC, the collector must have a lower work function than the emitter. Therefore, diamond has also been proposed as a low work function collector. Koeck and Nemanich produced a PDD collector with a work function of 0.67 eV.[35] Unless an alternative lower work function material gets proposed, TEC tests on a similar PDD collector can be designed. A suitable diamond emitter with a work function at least 1 eV higher than the collector can to be carefully produced to obtain a large work function difference.

5 Conclusion

In conclusion, two identical H-terminated BNDL diamond samples were produced. These samples were grown on a PCD wafer, which is why they consisted of randomly orientated diamond grains separated by graphitic grain boundaries. This morphology was observed by using SEM to analyse the surface of Sample 2. The work function map of Sample 2 produced by EF-PEEM revealed that on average these graphitic grain boundaries had a higher work function compared to diamond, even though the exact values of the work functions could not be determined due to charging. This non-uniform surface caused the electron emission properties of Sample 2 to vary across the surface, making it less efficient. Laser Raman spectroscopy on Sample 1 showed that the graphite peak at 1554.01 cm^{-1} for the NDL had a higher intensity than the BDL. Therefore, the NDL had more grain boundaries than the BDL, due to it having a shorter growth time.

The UPS spectrum of Sample 2 qualitatively confirmed the presence of an NEA in Sample 2, due the high intensity secondary electron peak which appeared at high binding energies. Due to charging, the exact value of the NEA, the work function or the energy of the VBM relative to the E_F could not be determined by UPS. XPS showed peaks at 285.47 eV and 286.21 eV corresponding to sp^3 diamond and sp^2 graphite, respectively. Despite the NDL layer at the surface, XPS was not able to detect the N 1s peak because the N content at the surface could have been below the XPS detection limit or due to an operational error. Therefore, in order to accurately characterise the composition and

electronic properties of Sample 2, the charging and detection limit issues must be resolved. To identify whether Sample 2 produced a n-type diamond needs to be confirmed with additional experiments such as Hall measurements and SIMS to determine whether the BN_2 and BN_3 clusters were formed between the doped layers.

The Ni-59 TEC tests showed an overall decrease in MECD over successive heating cycles. However, the MECD remained stable between cycle 3 and 8 due to regenerating H from the grain boundaries as the emitter was heated. These were able to bind to the surface C and preform H re-termination to maintain the NEA. The TEC test on the W collector also showed similar results, which confirmed that this H re-termination mechanism was likely to have occurred. However, after cycle 8 this effect ceased as the H re-terminated sites also desorbed in the Ni-59 test. Adding an additional 20 heating cycles could have allowed to observe when H completely desorbed to produce a PEA. On the other hand, for the Ni-63 tests the MECD increased overtime. This has been attributed to beta-enhancement. The high energy electrons released by the Ni-63 collector could have allowed for two beta-enhancement mechanisms to occur simultaneously. The first mechanism involved the beta particles skewing the Fermi-Dirac distribution of the emitter upon impact, allowing for more electrons with higher kinetic energies to be ejected from the emitter. The other mechanism could have occurred due to beta particles forcing more H atoms out of the grain boundaries to re-terminate the surface C more efficiently than just heating the emitter.

This research suggests that a Ni-63 collector could allow for TECs to operate with long operational lifetimes with minimal H desorption. However, more experiments are needed to see when or if the effects of beta enhancement come to an end. Nevertheless, the 6.27 enhancement factor obtained at the last heating cycle was high and could fuel further motivation to design TECs for sustainable energy generation using beta enhancement.

6 Appendix

The High Resolution O 1s peak

Since Sample 2 was quickly transported into a vessel containing Ar after H-termination, there was little oxidation observed at the surface, which is evident by the low intensity O 1s peak in Figure 1A.

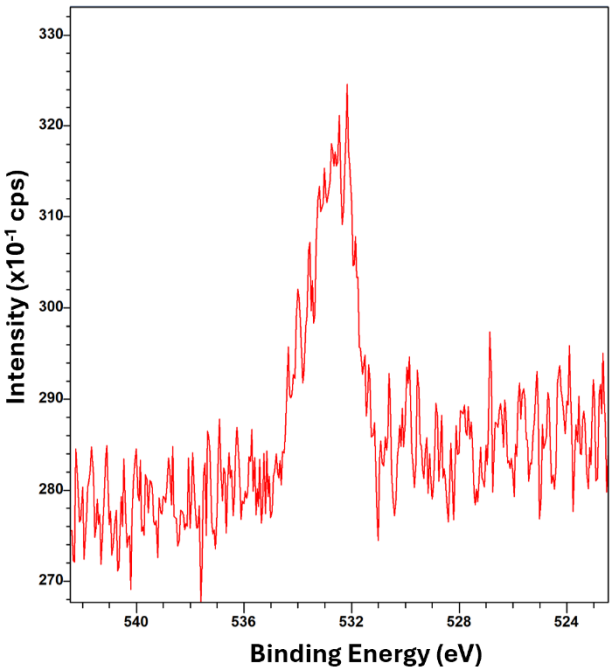

Figure A1 The high resolution XPS spectrum showing the O 1s peak of Sample 2.

7 References

1) International Energy Agency, https://www.iea.org/reports/electricity-2026/executive-summary, (accessed March 2026)
2) J. R. Smith, *J. Appl. Phys.*, 2013, **114**, DOI: https://doi.org/10.1063/1.4826202.
3) D. B. Go, J. R. Haase, J. George, J. Mannhart, R. Wanke, A. Nojeh, R. Nemanich, *Front. Mech. Eng.*, 2017, **3**, 1-15.
4) K. A. A. Khalid, T. J. Leong, K. Mohamed, *IEEE Trans. Electron Devices*, 2016, **63**, 2231–2241.
5) N. L. Allan, P. W. May, *Appl. Surf. Sci.*, 2026, **717**, 1-8.
6) B. Y. Moyzhes, T. H. Geballe, J. *Phys. D: Appl. Phys.*, 2005, **38**, 782–786.
7) M. F. Campbell, T. J. Celenza, F. Schmitt, J. W. Schwede, I. Bargatin, *Adv. Sci.*, 2021, **8**, 1-23.
8) K. H. Ng, L. S. Yuan, C. K. Cheng, K. Chen, C. Fang, *J. Clean. Prod.*, 2019, **233**, 210-220.
9) M. C. James, PhD thesis, University of Bristol, 2019.
10) F. Fogarty, N. A. Fox, P. W. May, *Funct. Diamond.*, 2022, **2**, 103–111.
11) P. Atkins, J. de Paula, J. Keeler, in *Elements of Physical Chemistry*, Oxford University Press, Oxford, 8th edn., 2025, ch. 12.
12) F. Huffman, in *Encyclopedia of Physical Science and Technology*, ed. R. A. Meyers, Academic Press, London, 3rd edn., 2003, pp. 627–638.
13) M. C James, F. Fogarty, R. Zulkharnay, N. A. Fox, *Carbon*, 2021, **171**, 532-550.
14) P. G. Tanner, D. A. Fraser, A. D Irving, *IEE Proc. Sci. Meas. Technol*, 2005, **152**, 1-6.
15) I. Bickerton, N. A. Fox, *Front. Mech. Eng.*, 2017, **3**, 1-4.
16) J. H. Lee, I. Bargatin, N. A. Melosh, R. T. Howe, *Appl. Phys. Lett.*, 2012, **100**, DOI: https://doi.org/10.1063/1.4707379.
17) H. Yuan, D. C. Riley, Z. X. Shen, P. A. Pianetta, N. A. Melosh, R. T. Howe, *Nano Energy*, 2017, **32**, 67–72.
18) A. Bellucci, M. Girolami, D. M. Trucchi, in *Ultra-High Temperature Thermal Energy Storage, Transfer and Conversion*, ed. A. Datas, Woodhead Publishing, Cambridge, 2021, ch. 10, pp. 253-284.
19) E. Rahman, A. Nojeh, *Phys. Rev. Appl.*, 2020, **14**, DOI: https://doi.org/10.1103/PhysRevApplied.14.024082.
20) M. Kamran, in *Renewable Energy Conversion Systems*, ed. M. R. Fazal, M. Kamran, Academic Press, Cambridge, 2021, ch. 2, pp. 21–51.
21) J. M. Houston, *J. Appl. Phys.*, 1959, **30**, 481–487.
22) P. A. Redhead, J. Vac. Sci. Technol. A., 1998, **16**, 1394–1401.
23) P. J. Angiolillo, *Am. J. Phys.*, 2009, **77**, 1102–1106.

24) The Nobel Prize, https://www.nobelprize.org/prizes/physics/1928/richardson/lecture/, (accessed October 2025).
25) A. V. da Rosa, in *Fundamentals of Renewable Energy Processes*, ed. A. V. da Rosa, Academic Press, London, 2nd edn., 2009, ch. 6, pp. 219-262.
26) Topaz International part II: The Transition to Collaboration, https://beyondnerva.wordpress.com/2019/03/22/topaz-international-part-ii-the-transition-to-collaboration/, (accessed March 2026)
27) S. Tang, H. Sun, C. Wang, W. Tian, S. Qiu, G. H. Su, T. Liu, *Prog. Nucl. Energy.*, 2019, **112**, 209–224.
28) J. W. Schwede, I. Bargatin, D. C. Riley, B. E. Hardin, S. J. Rosenthal, Y. Sun, F. Schmitt, P. Pianetta, R. T. Howe, Z. X. Shen, N. A. Melosh, *Nat. Mater.*, 2010, **9**, 762–767.
29) E. Rahman, A. Nojeh, *Nat. Commun.,* 2021, **12**, 1-7.
30) K. Kodihal, A Sagar, *J. Phys.: Conf. Ser.*, 2019, **1230**, 1-6.
31) M. B. Naseem, J. Lee, S. I. In, *Chem. Commun.*, 2024, **60**,14155-14167.
32) J. M. Skelton, *J. Mater. Chem. C*, 2021, **9**, 11772-11787.
33) W. Raja, P. Zilio, A. Alabastri, R. P. Zaccaria, J. Cunha, L. Summerer, T. W. Versloot, Photon-Enhanced Thermionic Emission, ESA, 2015.
34) G. Xiao, G. Zheng, M. Qiu, Q. Li, D. Li, M. Ni, *Appl. Energy*, 2017, **208**, 1318–1342.
35) F. A. M. Koeck, R. J. Nemanich, *Front. Mech. Eng.*, 2017, **3**, 1-9.
36) R.J. Narayan, R.D. Boehm, A.V. Sumant, in *Introduction to Medical Applications of Diamond Particles and Surfaces*, ed. R. J. Narayan, Woodhead Publishing, Cambridge, 2011, ch. 1, pp. 3-24.
37) P. W. May, *Phil. Trans. Roy. Soc. Lond.*, 2000, **358**, 473-495.
38) A. Persson, BSc thesis, University of Bristol, 2025.
39) K. G. Crawford, I. Maini, D. A. Macdonald, D. A. J. Moran, *Prog. Surf. Sci.*, 2021, **96**, 1-23.
40) J. J Gracio, Q. H. Fan, J. C. Madaleno*, J. Phys. D: Appl. Phys.*, 2010, **43**, 1-19.
41) H. J. Goldsmid, S. E. Goldsmid, *J. Phys. E: Sci. Instrum.,* 1979, **12**, 822-823.
42) W. De Boer, J. Bol, A. Furgeri, S. Müller, C. Sander, E. Berdermann, M. Pomorski, M. Huhtinen, *Phys. Status Solidi A.*, 2007, **204**, 3004–3010.
43) M. N. R. Ashfold, J. P. Goss, B. L. Green, P. W. May, M. E. Newton, C. V. Peaker, *Chem. Rev.*, 2020, **120**, 5745–5794.
44) S. B. Shirey, J. E. Shigley, *Gems Gemol.*, 2013, **49**, 188–222.
45) R. S. Balmer, J. R. Brandon, S. L. Clewes, H. K. Dhillon, J. M. Dodson, I. Friel, P. N. Inglis, T. D. Madgwick, M. L. Markham, T. P. Mollart, N. Perkins, G. A. Scarsbrook, D. J. Twitchen, A. J. Whitehead, J. J. Wilman, S. M. Woollard, *J. Phys.: Condens. Matter*, 2009, **21**, 1-20.
46) M. Afrasiabi, M. Roethlin, H. Klippel, K. Wegener, *Int. J. Solids Struct.*, 2022, **259**, 1-10.

47) M. Sultana, S. Karmakar, A. Haque, *Mater. Sci. Semicond. Process.*, 2025, **186**, 1-29.
48) A. Croot, PhD thesis, University of Bristol, 2018.
49) A. Tom, MSc thesis, University of Bristol, 2024.
50) C. Su, J. C. Lin, *Surf. Sci.*, 1998, **406**, 149–166.
51) T. L. Martin, PhD thesis, University of Bristol, 2011.
52) A. Martyanov, I. Tiazhelov, S. Savin, V. Voronov, A. Popovich, V. Sedov, *J. Cryst. Growth*, 2024, **648**, 1-7.
53) G. Conte, M. C. Rossi, S. Salvatori, F. Tersigni, P. Ascarelli, E. Cappelli, *Appl. Phys. Lett.*, 2003, **82**, 4459–4461.
54) C. J. H. Wort, R. S. Balmer, *Mater. Today.,* 2008, **11**, 22–28.
55) F. Zhao, Y. He, B. Huang, T. Zhang, H. Zhu, *Materials*, 2024, **17**, 1-43.
56) M. C. James, M. Cattelan, N. A Fox, R.F Silva, R. M Silva, P. W. May, *Phys. Status Solidi B.*, 2021, **258**, 1-13.
57) L. C. P. Charlo, PhD thesis, Universidad de Cadiz, 2016.
58) L. G. Wang, A. Zunger, *Phys. Rev. B*, 2002, **66**, DOI: https://doi.org/10.1103/PhysRevB.66.161202
59) D. Zhou, L. Tang, J. Zhang, R. Yue, Y. Wang, in *Computational Science – ICCS 2022*, ed. G. Derek, Springer International Publishing, Cham, 2022, pp. 530-540.
60) T. S. Almutairi, PhD thesis, University of Bristol, 2020.
61) A. I. M. Rahma, R. R. Swara, S. N. Zakiyyah, C. Y. Kharismasari, Z. Zhang, Y. Einaga, I. Kurnia, Y. W. Hartati, *Sens. Biosensing Res.*, 2025, **49**, 1-12.
62) X. Sun, D. Zhang, G. Wu, Q. Wang, C. Cheng, S. Liu, *Diam. Relat. Mater.*, 2025, **153**, 1-7.
63) P. W. May, W. J. Ludlow, M. Hannaway, P. J. Heard, J. A. Smith, K. N. Rosser, *Diam. Relat. Mater.*, 2008, **17**, 105–117.
64) H. Long, H. Hu, K. Wen, X. Liu, S. Liu, Q. Zhang, T. Chen, *Molecules,* 2023*, **28**,* 1-11.
65) M. Hu, N. Bi, S. Li, T. Su, Q. Hu, H. Ma, X. Jia, *CrystEngComm*, 2017, **19**, 4571–4575.
66) J. E. Moussa, N. Marom, N. Sai, J. R. Chelikowsky, *Phys. Rev. Lett.*, 2012, **108**, DOI: https://doi.org/10.1103/PhysRevLett.108.226404.
67) M. Z. Othman, P. W. May, N. A. Fox, P. J. Heard, *Diam. Relat. Mater.*, 2014, **44**, 1-7.
68) Y. Tominaga, A. Uchida, Y. M. Hunge, I. Shitanda, M. Itagaki, T. Kondo, M. Yuasa, H. Uestuska, C. Terashima, *Solid State Sci.*, 2024, **155**, 1-7.
69) A. Croot, M. Z. Othman, S. Conejeros, N. A. Fox, N. L. Allan, *J. Phys.: Condens. Matter.,* 2018, **30**, 1-9.
70) S. Koizumi, K. Watanabe, M. Hasegawa, H. Kanda, *Diam. Relat. Mater.*, 2002, **11**, 307–311.
71) D. Y. Liu, L. C. Hao, Y. Teng, F. Qin, Y. Shen, K. Tang, J. D. Ye, S. M. Zhu, R. Zhang, Y. D. Zheng, S. L. Gu, *APL Mater.*, 2021, **9**, DOI:10.1063/5.0049151.
72) R. Zulkharnay, PhD thesis, University of Bristol, 2023.

73) F. Maier, J. Ristein, L. Ley, *Phys. Rev. B*, 2001, **64**, DOI: https://doi.org/10.1103/PhysRevB.64.165411.
74) P. W. May, J. C. Stone, M. N. R. Ashfold, K. R. Hallam, W. N. Wang, N. A. Fox, *Diam. Relat. Mater.*, 1998, **7**, 671–676.
75) A. Rowan, MSc thesis, University of Bristol, 2017.
76) R. Zulkharnay, N. A. Fox, P. W. May, *Small*, 2024, **20**, 1-11.
77) R. Zulkharnay, W. Greenwood, A. Wood, J. Laverock, N. A. Fox, *ACS Appl. Mater. Interfaces*, 2026, **18**, 9032–9042.
78) J. Swarbrigg, MSc thesis, University of Bristol, 2025.
79) K. M. O'Donnell, M. T. Edmonds, A. Tadich, L. Thomsen, A. Stacey, A. Schenk, C. I. Pakes, L. Ley, *Phys. Rev. B*, 2015, **92**, DOI: https://doi.org/10.1103/PhysRevB.92.035303.
80) J. Navas, D. Araujo, J. C. Piñero, A. Sánchez-Coronilla, E. Blanco, P. Villar, R. Alcántara, J. Montserrat, M. Florentin, D. Eon, J. Pernot, *Appl. Surf. Sci.*, 2018, **433**, 408–418.
81) R. Zulkharnay, G. Zulpukarova, P. W. May, *Appl. Surf. Sci.*, 2024, **658**, 1-8.
82) D. B. Go, T. Musho, P. J. Shamberger, N. A. Fox, A. Croot, G. Wan, A. Rowan, H. D. Andrade, J. A. Smith, *Front. Mech. Eng.*, 2017, **3**, 1-7.
83) W. Ji, J. B. Kim, J. J. Kim, *Nucl. Eng. Technol.*, 2022, **54**, 3811–3815.
84) H. Bolton, MSc thesis, University of Bristol, 2019.
85) Element Six, https://e6cvd.com/us/application/thermal/tm100-10x10-mm-0-50-mm-thick.html, (accessed April 2026).
86) F. Fogarty, PhD thesis, University of Bristol, 2020.
87) Bruker,https://www.bruker.com/en/products-and-solutions/raman-spectroscopy/raman-basics/what-is-raman-spectroscopy/raman-spectrometer-optics.html, (accessed February 2026)
88) F. A. Stevie, C. L. Donley, *J. Vac. Sci. Technol. A*, 2020, **38**, DOI: https://doi.org/10.1116/6.0000412.
89) https://www.egr.msu.edu/cmsc/equipments/x-ray-photoelectron-spectrometer
90) P. D. Innes, *Proc. A,* 1907, **79**, 442–462.
91) J. E. Whitten, *Appl. Surf. Sci. Adv.,* 2023, **13**, 1-12.
92) T. Schultz, *Electron. Struct.,* 2022, **4**, 1-6.
93) B. J. Inkson, in Materials Characterization Using Nondestructive Evaluation (NDE) Methods, ed. G. Hübschen, I. Altpeter, R. Tschuncky, H. Herrmann, Woodhead Publishing, Cambridge, 2016, ch. 2, pp. 17-43.
94) S. Prawer, Robert J. Nemanich, *Philos. Trans. A. Math. Phys. Eng. Sci.,* 2004, **362**, 2537–2565.
95) D. L. Baptista, F. C Zawislak, *Diamond Relat. Mater.,* 2004, **13**, 1791-1801.
96) K. Teii, T. Ikeda, A. Fukutomi, K. Uchino, *J. Vac. Sci. Technol. B: Microelectron*, 2006, **24**, 263–266.
97) J. A. Pittard, M. Y. Lavrentiev, N. A. Fox, *Diam. Relat. Mater.,* 2024, **149**, 1-7.

98) S. Gupta, K. Bury, P. W. May, *Diam. Relat. Mater.,* 2026, **164**, 1-15.
99) R.S. Tsang, C.A. Rego, P. W. May, M.N.R. Ashfold, K.N. Rosser, *Diamond Relat. Mater.,* 1997*,* **6**, 247-254.
100) G. F. Zhang, D. S. Geng, Z. J. Yang, *Surf. Coat. Technol.*, 1999, **122**, 268–272.
101) J. Xu, K. Lu, D. Fan, Y. Wang, S. Xu, M. Kubo, *J. Phys. Chem. C.,* 2021, **125**, 16711–16718.
102) D. R. Baer, G. E. McGuire, K. Artyushkova, C. D. Easton, M. Engelhard, A. G. Shard, *J. Vac. Sci. Technol. A,* 2021*,* **39***,* DOI:10.1116/6.0000057/1063946.
103) R. Zulkharnay, P. W. May, *J. Mater. Chem. A Mater.*, 2023, **11**, 13432–13445.
104) S. Torrengo, L. Minati, M. Filippi, A. Miotello, M. Ferrari, A. Chiasera, E. Vittone, A. Pasquarelli, M. Dipalo, E. Kohn, G. Speranza, *Diam. Relat. Mater.*, 2009, **18**, 804–807.
105) L. Zhu, W. Li, L. Ma, X. Xu, J. Luo, *Laser Photonics Rev.*, 2024, **18**, DOI:10.1002/lpor.202301069.
106) P. Pearce, BSc thesis, University of Bristol, 2022.
107) Laser Displacement Sensors, https://www.keyence.eu/products/measure/laser-1d/, (accessed April 2026).
108) B. Ofuonye, J. Lee, M. Yan, C. Sun, J. M. Zuo, I. Adesida, *Semicond. Sci. Technol.*, 2014, **29**, DOI: 10.1088/0268-1242/29/9/095005.